

CAVITATION EROSION OF NICKEL ALUMINIDES

by
Raj P. Salvi, P.Eng. (Ont.)
Metallurgical Engineer, Indian Institute of Technology, Bombay,
India

A THESIS SUBMITTED IN PARTIAL FULFILLMENT OF
THE REQUIREMENTS FOR THE DEGREE OF
MASTER OF APPLIED SCIENCE

in

THE FACULTY OF GRADUATE STUDIES
(Department of Metals and Material Engineering)

We accept this thesis as conforming
to the required standard

THE UNIVERSITY OF BRITISH COLUMBIA
SEPTEMBER 1996

© Raj P. Salvi, P.Eng., 1996

In presenting this thesis in partial fulfilment of the requirements for an advanced degree at the University of British Columbia, I agree that the Library shall make it freely available for reference and study. I further agree that permission for extensive copying of this thesis for scholarly purposes may be granted by the head of my department or by his or her representatives. It is understood that copying or publication of this thesis for financial gain shall not be allowed without my written permission.

Department of Metals and Materials Engineering

The University of British Columbia
Vancouver, Canada

Date 30 Sept. 1996

ABSTRACT

Cavitation erosion is a major problem encountered in hydraulic machinery components. Presently, solution to the problem is sought through a two-fold approach of machine design and application of cavitation resistant materials. Stainless steels are commonly used for cavitation protection. Cobalt based alloys (stellites) and NiTi intermetallic compound are the best materials at present known to resist cavitation erosion. Physical and mechanical properties of various tested materials do not seem to correlate well with the cavitation erosion resistance of these materials.

The present study was done to investigate the cavitation erosion resistance of the intermetallic nickel aluminides Ni_3Al and NiAl . An ultrasonic (20 KHz) vibratory test apparatus was used to conduct tests with a modification to the ASTM G-32-92 method. The cavitation intensity and the surface finish were varied, from the specification, to investigate their effects on the cavitation erosion resistance of NiAl . Scanning electron microscopy and X-ray diffraction methods were used as aids in analyzing the results.

Unalloyed stoichiometric Ni_3Al was found to exhibit a higher cavitation erosion resistance than boron (0.2 wt. %) doped Ni_3Al . Alloying with boron imparts room temperature ductility to the otherwise brittle Ni_3Al compound. Investigations of deviation from stoichiometry were conducted on NiAl in the

compositional range of 47 - 62.2 at. % Ni in this work. The erosion rate was found to decrease monotonically with increasing nickel content, in the range tested. Strain induced martensitic transformation was found to be associated with the compositions which showed the low cavitation erosion rates. Thermally induced martensite which was present in these compositions, was found to be detrimental to the cavitation erosion resistance of NiAl.

NiAl compositions of 58 at. % Ni and 62.2 at. % Ni showed cavitation erosion resistance comparable to that of the best known intermetallic NiTi. However, in terms of materials processing NiAl offers advantages over NiTi. Hence NiAl could find a niche as an industrially important material for cavitation protection of hydraulic machinery. The most desirable NiAl compositions exhibit unusual but desirable variations of erosion rate with cavitation intensity. Further studies are needed for a better understanding of this phenomenon.

Table of Contents

ABSTRACT	ii
Table of Contents	iv
List of Tables	v
List of Figures	vi
ACKNOWLEDGMENTS	xi
1.0 INTRODUCTION, OBJECTIVE AND SCOPE OF THE STUDY	1
2.0 BACKGROUND ON NICKEL ALUMINIDES	5
2.1 Physical and Mechanical Properties	9
2.2 Deformation Modes and Fracture Behaviour	16
2.3 Martensitic Transformation	20
2.3.1 Shape Memory Effect	25
2.3.2 Strain Induced Transformation	30
2.3.3 Deformation of Strain Induced Martensite	34
3.0 EXPERIMENTAL WORK	36
4.0 RESULTS AND OBSERVATIONS	43
5.0 DISCUSSION	66
6.0 CONCLUSIONS	85
7.0 FUTURE DIRECTION	87
REFERENCES	88

List of Tables

Table I	Tensile Properties of Ni ₃ Al at Room Temperature	9
Table II	Variation in Physical Properties due to Deviations from Stoichiometry of Ni ₃ Al	10
Table III	Tensile Strength and Hardness Variation with Compositions for NiAl at Room Temperature	13
Table IV	Composition of Test Samples	41
Table V	Mechanical Properties and Cavitation Erosion Rate for Stoichiometric Ni ₃ Al	71
Table VI	Cavitation Erosion Rate of NiAl in the composition range of 47 - 62.2 at. % Ni	72
Table VII	Cavitation Damage Resistance of Various Materials	73
Table VIII	Incubation period of Stoichiometric and non-Stoichiometric NiAl	79
Table IX	Erosion Rates	81

List of Figures

Figure 1	The Ni-Al phase diagram	5
Figure 2	Ni ₃ Al and NiAl structures	6
Figure 3	Thermal conductivity of Ni base superalloys and NiAl	7
Figure 4	Hardness change of NiAl with composition	8
Figure 5	Variations of lattice parameter and density with composition in NiAl	11
Figure 6	Variation of tensile strength with composition for NiAl	12
Figure 7	Variation of NiAl elastic modulus with orientation and temperature	14
Figure 8	Orientation effect on elastic modulus in polycrystalline NiAl	15
Figure 9	Variation of fracture toughness with orientation for NiAl	18
Figure 10	Lattice correspondence and CsCl structure transformation to fct or CuAuI structure in martensitic transformation	20
Figure 11	Shear deformation by slip or twinned substructure in martensite variant	21
Figure 12	A _s and A _f temperatures for martensitic transformation	22
Figure 13	Au 47.5 at. % Cd alloy showing transformation front	23
Figure 14	Twin density variation with nickel content in NiAl	24
Figure 15	Shape memory effect in martensitic transformation	25

List of Figures (cont.)

Figure 16	Stress-strain curve for Cu-Zn showing reduced stress required as M_s temperature is approached	27
Figure 17	Linear relationship of the Clausius-Clapeyron equation in the case of Cu-Zn alloy	28
Figure 18	Stress-strain diagram for materials showing SE	30
Figure 19	Schematic representation for thermoelastic nature of martensite in NiAl	31
Figure 20	Crystal orientation effect for stoichiometric NiAl	32
Figure 21	Schematic casting set up for Ni ₃ Al bar casting	36
Figure 22	Hardness readings along the bar length for Ni ₃ Al	37
Figure 23	EDXA results for Ni ₃ Al bar	37
Figure 24	Hardness readings after homogenization anneal for Ni ₃ Al	38
Figure 25	Schematic of the cavitation test apparatus	39
Figure 26	NiAl bars procured from Oakridge National Laboratories with different nickel percentages	41
Figure 27	SEM photograph of spheroidized carbon in Ni ₃ Al bar (34,00X)	43
Figure 28	EDX pattern of carbon nodule	43
Figure 29	SEM photograph of cracks in Ni ₃ Al sample (20X)	44
Figure 30	Cavitation erosion mass loss rate curve of Ni ₃ Al (cracked sample)	45
Figure 31	Ni ₃ Al (cracked) sample after 24 hours of testing (50X)	45

List of Figures (cont.)

Figure 32	SEM photograph of persistent slip bands with microvoids in Ni ₃ Al (cracked) sample after 24 hours of cavitation testing (5.00 K)	46
Figure 33	Cavitation erosion mass loss curve for Ni ₃ Al (uncracked sample)	47
Figure 34	SEM photograph showing fatigue striations in Ni ₃ Al during cavitation erosion	47
Figure 35	SEM photograph of Ni ₃ Al (uncracked sample) after 24 hours of cavitation erosion plastic deformation	48
Figure 36	Cavitation erosion mass loss curve for 47 at. % Ni-NiAl	49
Figure 37	Grain boundary fracture in 50 at. % Ni seen during Rockwell 'C' hardness testing (50 X)	50
Figure 38	SEM photograph of 50 at. % Ni fracture surface (200X)	50
Figure 39	Cavitation erosion mass loss curve for 50 at. % Ni	51
Figure 40	Cavitation erosion mass loss curve for 53 at. % Ni	52
Figure 41	Single grain of 53 at. % Ni during different stages of cavitation (200X)	52
Figure 42	XRDA graph for 58 at. % Ni uncavitated sample	53
Figure 43	Microphoto showing presence of thermal martensite in 58 at. % Ni as cast sample in uncavitated condition (500X)	54
Figure 44	Cavitation erosion mass loss curve for 58 at. % Ni	54
Figure 45	Strain induced martensite transformation observed during cavitation testing of 58 at. % Ni (1000X)	55
Figure 46	Graph showing dependence of orientation with strain in NiAl martensite	56

List of Figures (cont.)

Figure 47	Cavitation erosion mass loss curve for 58 at. % Ni tested at $\pm 25 \mu\text{m}$ amplitude and 600 grit surface finish	56
Figure 48	Cavitation erosion mass loss curve for 58 at. % Ni tested at $\pm 25 \mu\text{m}$ and $0.05 \mu\text{m}$ surface finish	57
Figure 49	Variation of intensities of major peaks in 58 at. % Ni during cavitation erosion	58
Figure 50	Optical microphoto of 58 at. % Ni during cavitation erosion testing for 6 hours (1000X)	58
Figure 51	Microphotos of 58 at. % Ni showing erosion after (a) 10 hours, (b) and (c) 14 hours. Micrograph (d) is taken from ref. [35] (1000X)	59
Figure 52	Cavitation erosion mass loss curve for 62.2 at. % Ni with $\pm 16 \mu\text{m}$ test amplitude and 600 grit finish	60
Figure 53	Microphoto showing presence of thermal martensite in 62.2 at. % Ni as cast sample in uncavitated condition (500X)	61
Figure 54	Cavitation erosion mass loss curve for 62.2 at. % Ni with $\pm 25 \mu\text{m}$ and 600 grit surface finish	61
Figure 55	Occurrence of major erosion in grit marks as compared to grain boundaries (1000X)	62
Figure 56	Cavitation mass loss for 62.2 at. % Ni with $\pm 25 \mu\text{m}$ test amplitude and $0.05 \mu\text{m}$ surface finish	63
Figure 57	Strain induced martensite after 10 hours of cavitation testing in 62.2 at. % Ni sample (1000X)	63
Figure 58	SEM photograph of a single grain in 62.2 at. % Ni after 10 hours of cavitation testing	64
Figure 59	Optical microphoto showing homogeneously formed strain induced martensite in 62.2 at. % Ni sample during cavitation testing (500X)	64

List of Figures (cont.)

Figure 60	XRD graphs at different time periods for 62.2 at. % Ni during cavitation erosion	65
Figure 61	Variation of mass loss rate due to cavitation erosion in NiAl with atomic percent nickel	68
Figure 62	M _s temperature variation with atomic percent nickel in NiAl	70
Figure 63	Variation of tensile strength and cavitation erosion rate with atomic percent nickel	72
Figure 64	Variation of incubation period with nickel content in NiAl for 600 grit surface finish and ±16 μm test	79
Figure 65	Effect of cavitation intensity and surface finish on mass loss rate for 47-62.2 at. % Ni in NiAl	80
Figure 66	Variation of erosion rate with cavitation intensity for alloys	82
Figure 67	Comparison of cavitation erosion rates for tested industrial alloys tested for cavitation erosion by the stationary specimen method	83

ACKNOWLEDGMENTS

The author would like to express his gratitude and thanks to his supervisor, Dr. Ainul Akhtar for his advice, expertise and encouragement during the course of the project. Special thanks are extended to Dr. V. K. Sikka of Oak Ridge National Laboratories, Tennessee, U.S.A. for supplying the NiAl samples used in this investigation. Thanks are also extended to the faculty, staff and fellow graduate students in the Department of Metals and Materials Engineering. Financial assistance from NSERC is gratefully acknowledged.

1.0 INTRODUCTION, OBJECTIVE AND SCOPE

Cavitation erosion occurs in a variety of hydraulic machinery components such as valves, cylinder liners of diesel engines, propellers of ships, impellers of hydraulic pumps, and hydraulic turbines in power generation. This causes reduction in peak performance of these machines due to:

- (1) Reduction in life span;
- (2) Loss of reliability and availability of the equipment; and
- (3) Lowering of the efficiency.

Considering that 60% of electric power was generated in Canada during 1991 using hydraulic turbines [1] and that a growth in hydraulic power of 31% is projected by the year 2010, cavitation erosion studies are needed.

Cavitation is caused by the fluid being subjected to abrupt pressure changes. Vapour filled voids or cavities are formed at low pressure regions in the liquid [2]. Flow patterns or vibrations in the system cause pressure differences causing the nucleation, growth and collapse of these cavities. When the pressure falls below the vapour pressure of the liquid, cavities are generated and move along the fluid flow till they encounter a high pressure region where they collapse and emit shock waves repeatedly with up to 2000 MPa pressure [3] which are sufficient to cause localized fracture of most structural materials. Machinery design can prevent collapse of these cavities near the metal surface.

However, due to variations in operating conditions such as water head below

the design level caused by drought conditions, there may be cavitation erosion. Hence good materials which have high cavitation resistance are needed.

The entire equipment can be made using such cavitation resistant materials to minimize the cavitation erosion, but it may make economic sense only in some applications. Generally only critical cavitation prone areas or components are made with cavitation resistant materials.

Metallic, composite, polymeric, and ceramic materials have been evaluated for cavitation erosion in the past [4, 5]. Although ceramic and polymeric materials show excellent cavitation resistance, there remain problems associated with their interfacing to the substrate. Composite materials also exhibit good cavitation erosion resistance but are still under a process of development.

Metallic structural materials commonly used are carbon steels and martensitic stainless steels. The latter has better cavitation erosion resistance [6]. Hence martensitic stainless steels with 13% chromium and up to 4% nickel have been used in the past 20 years with a variety of hydraulic machines. Austenitic 18-8 stainless steels exhibit superior cavitation resistance to martensitic stainless steels but due to their high cost, they are used for the construction of the entire component in special cases only.

Systematic studies have been made of stainless steels, duplex stainless steels and cobalt based alloys in the past to understand the micromechanics of the

deformation process as they relate to composition and microstructure of the alloys [6, 7].

Cobalt based alloys like Stellite 6B show the lowest cavitation erosion rate among the metallic materials. Stellite 6B was found to exhibit a stress induced martensitic transformation [60]. However, cobalt is an environmentally hazardous material, becoming radioactive when used in nuclear turbine applications and is also undesirable in downstream water emerging from hydro turbines. Hence there is need to develop other alloys which could show comparative or better cavitation erosion resistance than Stellite 6B alloy.

Ni₃Al microalloyed with boron has been studied for its cavitation erosion resistance. The alloy shows better resistance than Stellite 21 alloy [63]. However, the room temperature stability of Ni₃Al compositional range is extremely narrow as seen in Fig. [1] making it difficult to control composition in practical applications.

NiAl has a wide compositional range over which it is stable at 400°C. It can be processed by conventional methods of manufacture. It exhibits a stress induced martensite (SIM) transformation on application of stress, and is also cheaper than Ni₃Al because of reduced nickel percentage.

The present investigation was undertaken to find the cavitation erosion resistance of Ni₃Al and NiAl for deviations from stoichiometry. However, considering the narrowness of the stable compositional range for Ni₃Al it was

decided to study the cavitation erosion response only for the stoichiometric Ni_3Al . The study of cavitation erosion resistance of NiAl for deviations from stoichiometry would:

- (1) Classify NiAl for its cavitation erosion resistance with other materials.
- (2) Identify the NiAl composition which shows the highest cavitation erosion resistance.
- (3) Establish mechanisms of failure of the NiAl as it erodes.
- (4) Help suggest methods to increase its cavitation erosion resistance.

NiAl compositions with the maximum cavitation erosion resistance could then be used for the protection of hydraulic machinery.

The NiAl phase has a CsCl or B_2 structure. A similar intermetallic compound NiTi is reported to have good cavitation erosion resistance [8]. However, NiTi becomes meta-stable at 600°C resulting in a martensite phase at room temperature [9]. Stoichiometric NiTi shows low cavitation erosion rates comparable to Stellite 6B alloy. It also exhibits a stress-induced martensite transformation [60] and has a very narrow compositional range over which it is stable at room temperature. NiTi also requires special and expensive manufacturing methods. These factors limit the practical application of NiTi as a cavitation erosion resistant material. The NiAl phase remains stable at room temperature over a wide compositional range hence cavitation erosion resistance could be studied over a wide range of deviation from stoichiometry.

2.0 BACKGROUND ON NICKEL ALUMINIDES

Fig. [1] shows the phase diagram for the aluminum nickel system. Several intermetallic compounds are found in this system. Two of these Ni_3Al and NiAl are of industrial significance. These phases show ordered crystal structures of the AuCu_3 (I_2 or CP_4) and CsCl (B_2 or CP_2) type respectively [10] as shown in Fig. [2].

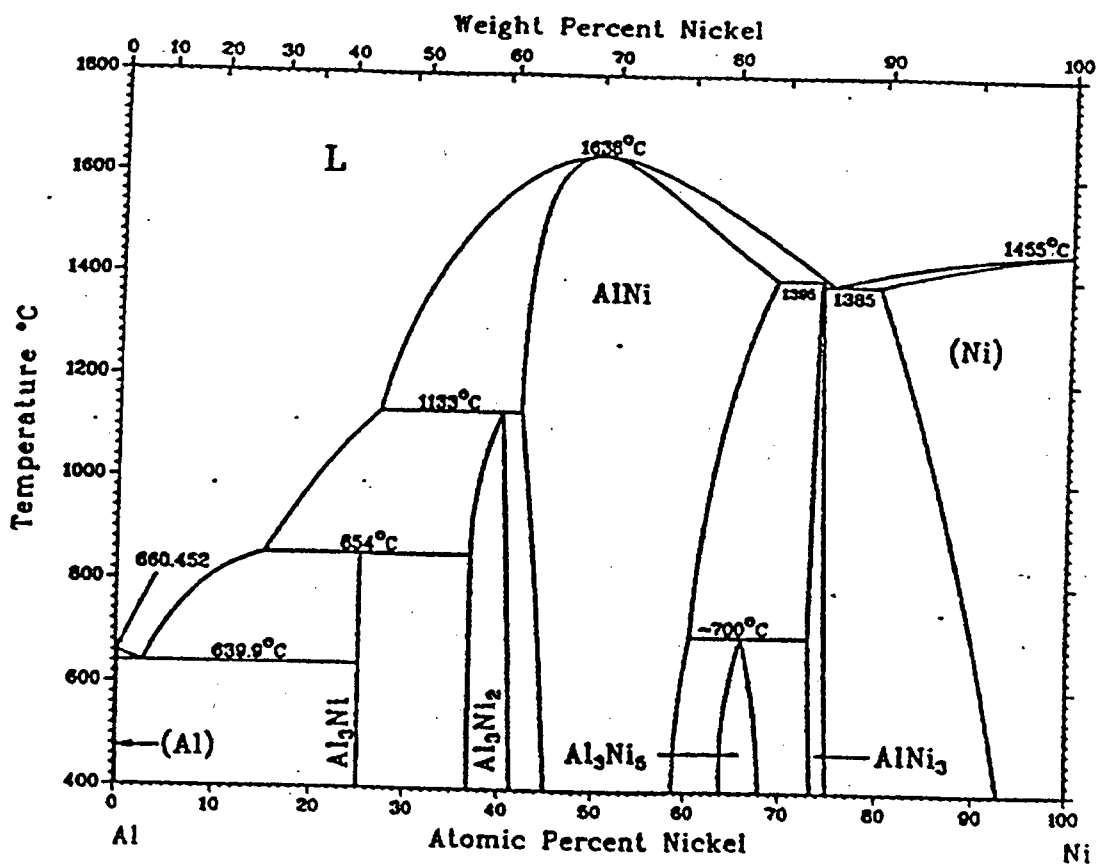


Figure [1] - The Ni-Al phase diagram - Ref. (Metals Handbook Vol. 3)

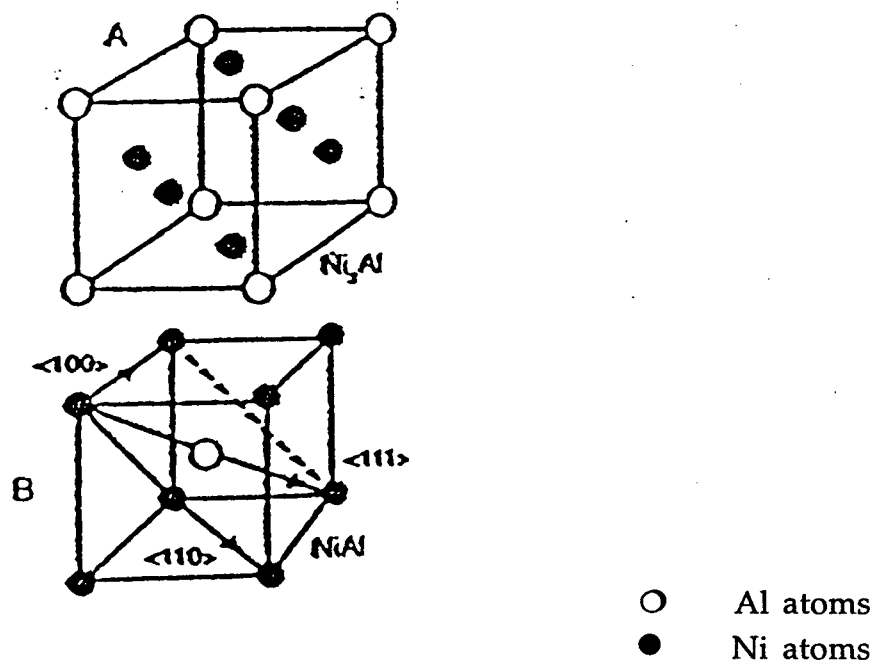


Figure [2] - Ni_3Al and NiAl structures - Ref. [13]

The ordered structures remain stable even at high temperatures as seen in the phase diagram. The yield strength of Ni_3Al increases with temperatures up to 750°C [11]. The intermetallic compound Ni_3Al is found as the γ' phase which gives good creep resistance properties to Ni-based superalloys [12]. Both these aluminides show low densities in the range of 5 - 6 g./ml. [13] with thermal conductivities as high as eight times those of Ni base superalloys as shown in Fig. [3]. These properties make Ni_3Al and NiAl good structural

materials for aerospace applications.

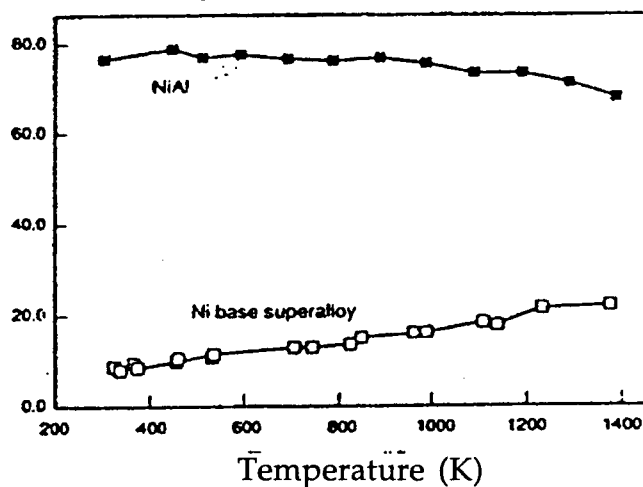


Figure [3] - Thermal conductivity of Ni base superalloys and NiAl - Ref. [13]

Although the nickel aluminides can be processed by conventional processing methods such as casting, extrusion, electro slag refining (ESR) or directional solidification, they are extremely brittle at room temperature. Nickel aluminides also exhibit anisotropic elastic and plastic behaviour. Their fracture toughness values are generally in the range of 8 - 10 MPa m^{1/2}. Ductility has been increased either by alloying or grain size refining [14, 15].

Vacancy concentration and migration play a significant part in the mechanical and physical properties of nickel aluminides [14]. Deviation from stoichiometry induces two types of defects in these intermetallics, one being a structure defect (SD), the other anti-structure defect (ASD) [16]. At its stoichiometric composition NiAl (CsCl structure), the nickel atoms remain located at the corners while the aluminum atoms remain at the centre of the crystal lattice unit cell. Aluminum atoms in excess of the stoichiometric

level leave some of the nickel sites vacant causing a structure defect (SD) and leading to lattice distortion. For compositions with fewer aluminum atoms, the excess of nickel atoms occupy the aluminum sites causing an anti-structure defect (ASD) and an associated lattice distortion again. Hence, both deviations from stoichiometry in NiAl lead to increased hardness, with stoichiometric nickel aluminide having the lowest hardness, as shown in Fig. [4].

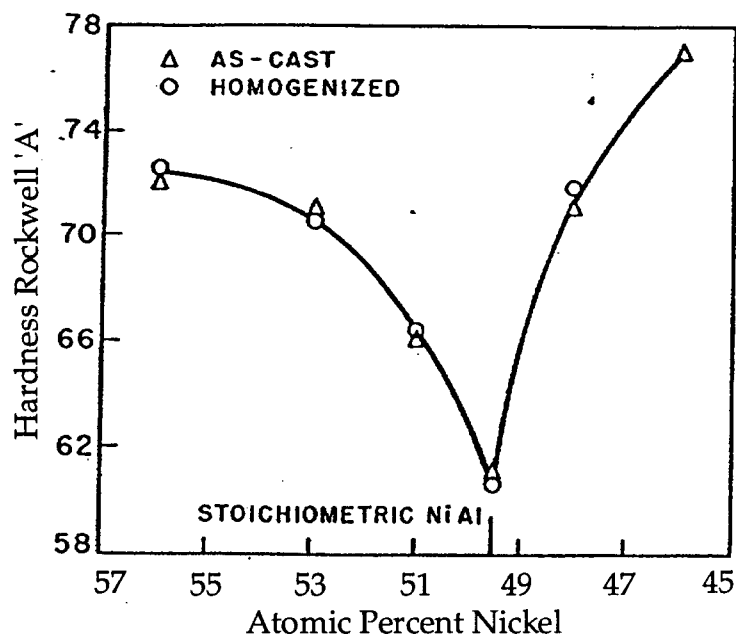


Figure [4] -Hardness change of NiAl with composition - Ref. [17]

The intermetallic compound NiAl also exhibits a shape memory effect (SME) in the composition range 60 at. % Ni ~ 69 at. % Ni. Thermo-elastic martensite (TM) starts forming at these compositions at temperatures between 100°K to 1200°K [9]. Strain induced martensite (SIM) transformation is also observed in NiAl [10].

2.1 PHYSICAL AND MECHANICAL PROPERTIES

Ni₃Al:

As seen in the phase diagram shown in Fig. [1], this compound remains stable at room temperature in the range 74 at. % Ni to 76 at. % Ni. For the stoichiometric composition Ni₃Al (75 at. % Ni and 25 at. % Al) the melting point is 1385°C. The lattice parameter of the stoichiometric Ni₃Al is 3.58Å.

Single crystal Ni₃Al exhibits tensile ductility figures up to 20% [20]. However cast, polycrystal Ni₃Al shows intergranular fracture at room temperature with ductility as low as 1 - 2%. This is due to the low cohesive strength of the grain boundaries in the ordered Ni₃Al. Additions [21, 22] in the range of 0.2 - 0.5% boron and control of aluminum composition below the stoichiometric level of 25 at. % Al, increases the ductility of Ni₃Al to above 30%. Boron has been found to segregate to the grain boundaries. This segregated region which has a width of about 1.5 μm and a disordered structure [23] permits easier slip movement of dislocations [24].

The room temperature tensile properties of Ni₃Al are shown in Table [I].

Composition at. % Ni	Condition	Yield Strength psi	Tensile Strength psi	Extensometer Elongation %
75	As-cast	12,000	30,600	1.1
		13,000	26,700	.9
75	Homogenized at 980°C for 48 hr.	10,000	22,200	0.2
		12,500	18,500	.2
74	As-cast	15,000	50,600	1.7
			45,900	
74	As-cast	15,500	39,500	1.2
		14,000	39,000	1.2
74	Homogenized at 980°C for 48 hr.	22,000	32,100	0.4
		21,000	32,100	.4
74	Homogenized at 1205°C for 48 hr.	22,500	26,600	0.1
		21,000	25,900	.2

1 psi ≡ 6.894 kPa

The tensile strength variation with deviation from stoichiometry is also included in Table [I]. The elastic modulus for Ni₃Al at room temperature is found to be the same as that of pure nickel but the rate of decrease of elastic modulus with increasing temperature for Ni₃Al remains one half that of pure nickel [25]. Table [II] shows the variations of other properties with respect to deviation from stoichiometry in Ni₃Al. The coefficient of thermal expansion does not show a significant change with composition.

Table II - Ni ₃ Al Variation of Physical Properties for Deviations from Stoichiometry Ref. [17]				
Temp. K	Electrical Resistivity 10 ⁸ Ωm	Thermal Conductivity Wm ⁻¹ K ⁻¹	Absolute Seebeck Coefficient, μV K ⁻¹	Thermal Expansion Coefficient 10 ⁶ K ⁻¹
Ni _{0.75} Al _{0.25}				
4.2	1.54
300	32.59	28.85	+5.4	12.5
400	39.00	33.72	+4.1	13.0
500	44.75	35.13	+1.8	13.5
600	50.13	36.18	-0.4	14.0
700	55.27	37.07	-2.4	14.6
800	60.54	37.27	-4.3	15.2
900	66.50	36.86	-5.5	16.0
1000	73.02	36.12	-6.3	16.8
Ni _{0.76} Al _{0.24}				
4.2	9.05
300	51.3	21.37	+9.9	12.5
400	58.89	24.21	+10.8	13.2
500	64.17	26.35	+7.9	13.8
600	68.60	28.30	+5.1	14.3
700	72.60	30.14	+2.3	14.8
800	76.52	31.82	-0.4	15.4
900	80.41	33.13	-2.8	16.1
1000	84.24	32.70	-4.8	16.8

Ordered Ni₃Al exhibits high strain hardening rates that are comparable to disordered FCC alloys.

NiAl:

The nickel-aluminum system phase diagram in Fig. [1] shows that this phase has a wide compositional range from 43 at. % Ni to 65 at. % Ni over which it is stable at room temperature.

Stoichiometric NiAl has a high melting point of 1638°C. The lattice parameter and density vary with deviation from stoichiometry. These are shown in Fig. [5].

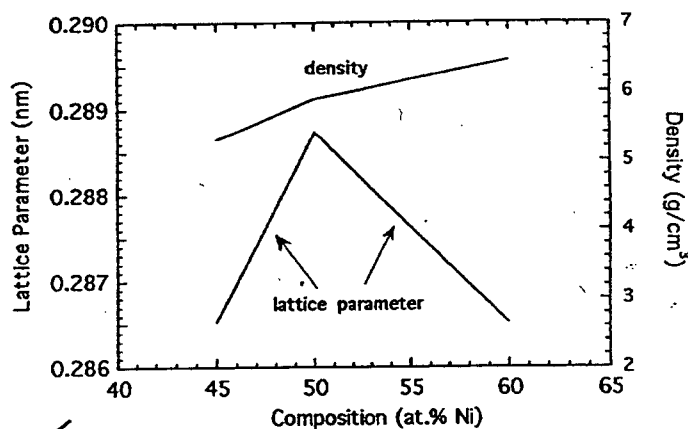


Figure [5]-Variation of lattice parameter and density with composition - Ref. [26]

The physical and mechanical properties of ordered NiAl are sensitive to deviation from stoichiometry [26]. The variation of tensile strength with a change in composition of NiAl at room temperature is shown in Table [III] and Fig. [6]. Table [III] also shows the change in hardness with deviations from stoichiometry. The hardness is a minimum at the stoichiometric composition. Vedula and Khadikar have shown that yield strength

shows a minimum at the stoichiometric composition. [27].

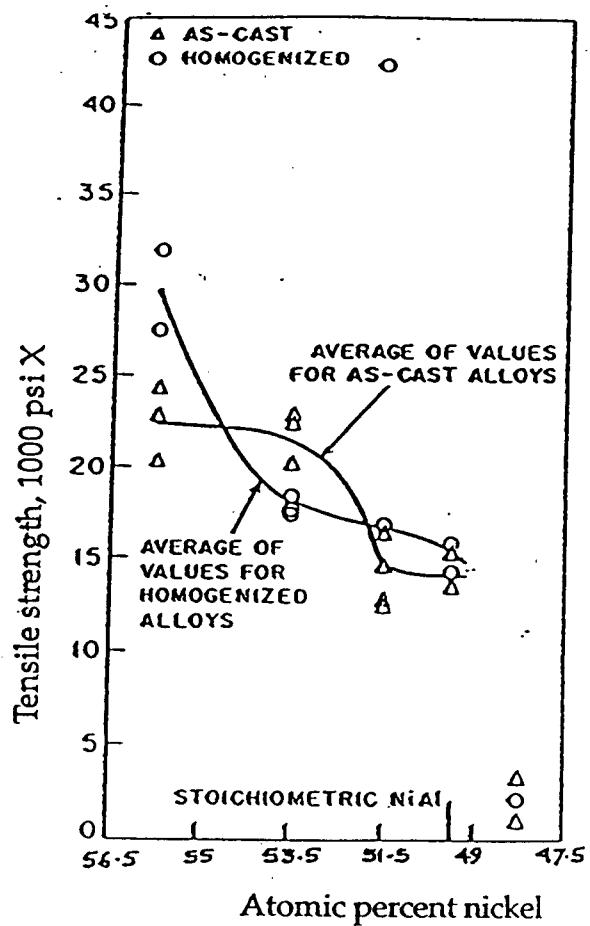


Figure [6] - Variation of tensile strength with composition for NiAl - Ref. [17]

Table III - Tensile Strength and Hardness Variation with Composition at Room Temperature for NiAl - Ref. [17]							
Composition at. % Ni	Condition	Tensile Strength psi	Extensometer Elongation %	Measured Elongation %	Hardness Rockwell A	Density g/cc	Lattice Parameter, kX Units
57	As-cast	22,700	0	0	72.0	6.40	...
	As-cast	24,100	0	0	72.0	6.33	...
	As-cast	20,200					
57	Homogenized at 1150°C for 48 hr.	31,800 27,100	0 0	0 0	72.5	6.37	...
54	As-cast	22,600	0	0	69.7	6.16	...
	As-cast	20,000	0	0	71.0	6.12	...
	As-cast	22,400	0	0			
54	Homogenized at 1205°C for 48 hr.	18,200 17,500	0 0	0 0	70.6	6.15	...
52	As-cast	14,400	0	0	66.1	5.99	2.88
	As-cast	16,300	0	0	...	5.98	
	As-cast	12,500	0	0			
52	Homogenized at 1315°C for 48 hr.	42,200 16,700	0	0	66.3	6.03	2.88
50	As-cast	15,200	0	0	61.0	5.93	2.88
	As-cast	13,300	0	0			
	As-cast	Unsound ingot	5.89	...
50	Homogenized at 1205°C for 48 hr.	15,700 14,100	0 0	0 0	60.6	5.93	2.88
48	As-cast	3,000	0	0	71.0	5.72	...
		1,400	0	0			
48	Homogenized at 1150°C for 48 hr.	1,860	0	0	71.8	5.70	...
46	As-cast	Unsound ingot	77.0

1 psi = 6.984 kPa

The elastic properties of single crystal NiAl have been found to be anisotropic with an anisotropy factor $A=2C_{44}/(C_{11} - C_{12})$ at room temperature [28]. This factor suggests a strong dependence on grain orientation in NiAl. Fig. [7] shows the variation of Young's modulus with temperature for three different crystal orientations.

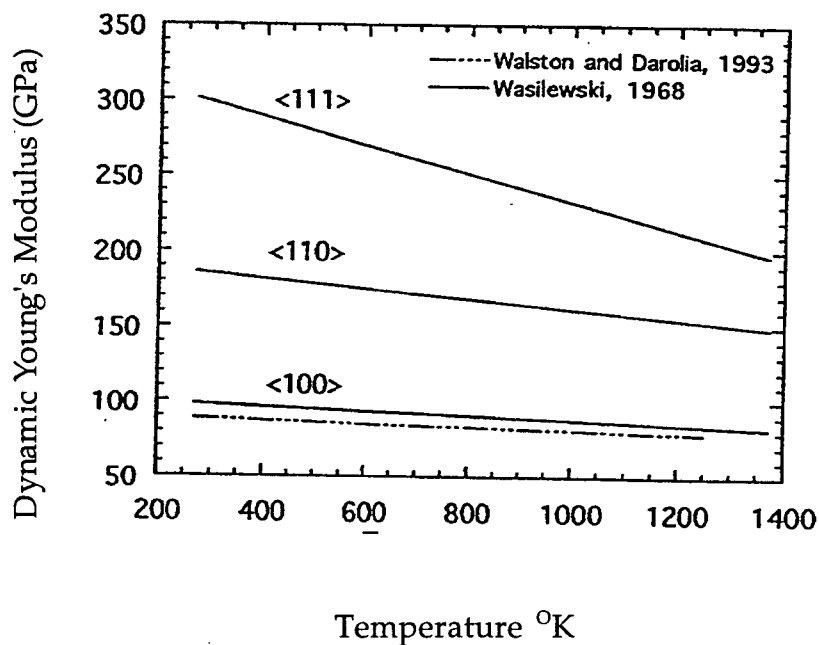


Figure [7] - Variation of NiAl elastic modulus with orientation and temperature - Ref. [26]

However, the modulus of polycrystalline NiAl depends upon the method of production of the compound. This is indicated in Fig. [8]. It is observed that extruded NiAl shows a higher elastic modulus than a conventional cast or hot-pressed pre-alloyed powder. The extruded NiAl shows a preferred <111> orientation whereas the cast or hot-pressed pre-alloyed powder does not show any preferred orientation.

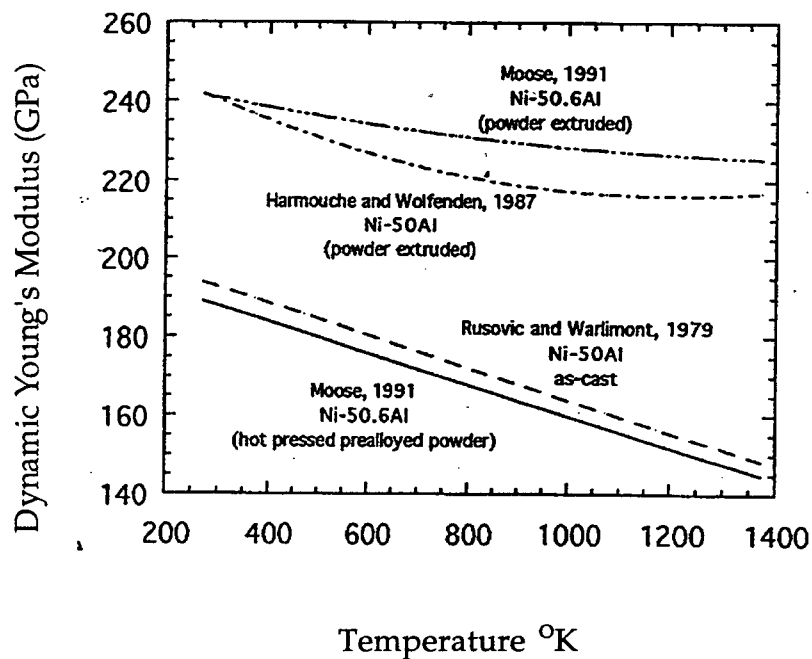


Figure [8] - Orientation effect on elastic modulus in polycrystalline NiAl - Ref. [26]

NiAl exhibits a brittle-to-ductile transition temperature (BDTT) at 600°K - 900°K, leading to practically nil ductility at room temperature [29] in the usual grain size range of polycrystalline materials. This has been attributed to an insufficient number of slip systems available to satisfy Von Mises criterion [30] for plasticity.

2.2 DEFORMATION MODES AND FRACTURE BEHAVIOUR

Ni₃Al:

Crystallographic slip is the observed mode of deformation in this intermetallic compound. However, deformation of Ni₃Al is a major problem because it shows room temperature brittleness due to weak grain boundary cohesive strength. As mentioned earlier boron addition and control of composition to hypostoichiometric deviation has been able to impart room temperature ductility in Ni₃Al.

The increase in ductility of Ni₃Al is caused due to boron segregating to the grain boundary, inducing a localized region of disorder at the boundary, making the slip of dislocations across the grain boundary easier. This slip is competitive with crack initiation leading to transgranular or intergranular fracture [25]. Slip in polycrystalline Ni₃Al at low temperatures occurs on {111} plane by glide of a superdislocation comprised of two partial dislocations of the type $1/2 \langle 110 \rangle$. At higher temperatures and strain rates, slip occurs on the {100} planes in the $\langle 110 \rangle$ directions [25].

On cooling from high temperature, the ordered structure becomes tetragonal and this increases the misfit between the parent cubic phase leading to high stresses in the lattice [31].

A high value of antiphase boundary energy (APB) implies the need for a high driving force. Ordered Ni₃Al is found to work harden rapidly as cross slip of

the superdislocation does not occur due to a high APB energy ratio. Low energy superlattice intrinsic stacking faults are observed in polycrystalline Ni₃Al deformed under compression at room temperature [32]. There has been no evidence of other modes of deformation such as twinning or transformation observed in ordered polycrystalline Ni₃Al.

Since slip remains the only deformation mode operative in polycrystalline Ni₃Al, the presence of persistent slip bands (PSB's) will play a significant part in the fracture initiation process in this compound when subjected to cyclic deformation, as in the case of cavitation erosion. Stoloff [33] has observed {111} primary slip bands which were thin and dense at early stages of high cycle fatigue and then coarsened into PSB-like bands. Eventually distinct stage I cracks on {111} were observed. Microvoids were observed to act as crack initiation sites indicating that condensation of point defects play an important part in the fracture of Ni₃Al.

NiAl:

NiAl single crystals exhibit two different types of slip behaviour depending upon crystal orientation. Crystals subjected to tensile stress along a <100> axis are termed "hard" due to their high flow stress and those with applied stress along all non <100> axes are referred to as "soft" crystals.

In the "soft" orientation <100> slip occurs whereas in "hard" orientations the slip direction becomes <111>. NiAl single crystals in "soft" orientation

deform by $\langle 001 \rangle$ slip on either $\{100\}$ or $\{110\}$ slip planes in accordance with Schmid's law. "Hard" orientations do not obey Schmid's law because $\langle 001 \rangle$ $\{100\}$ Burgers vectors have a zero or near zero resolved critical shear stress (τ_{crss}) resulting in the operation of alternative slip system in $\langle 011 \rangle$ $\{100\}$ at very large yield stresses [26]. Fracture toughness values for single crystals show anisotropic values for different orientations [30] as shown in Fig. [9].

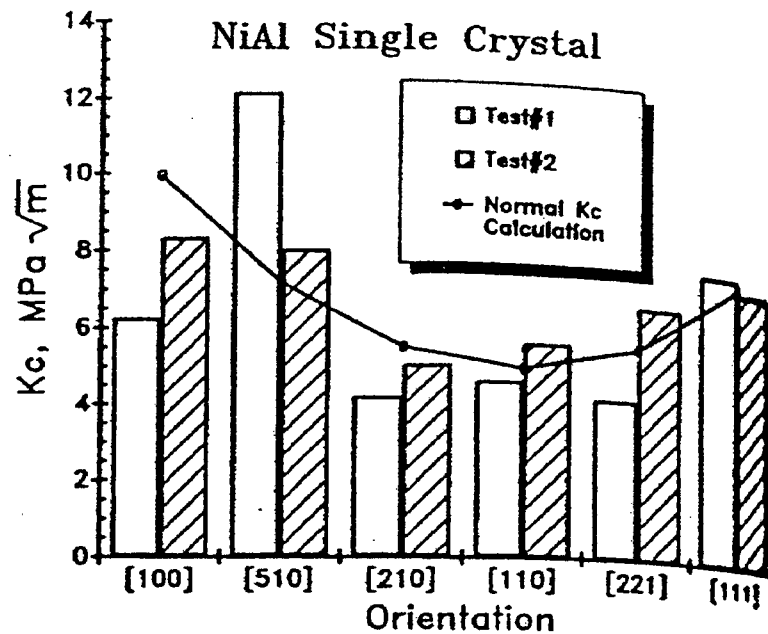


Figure [9] - Variation of fracture toughness with orientation for NiAl - Ref. [64]

The NiAl polycrystals deform similar to "soft" orientations in single crystals. Polycrystalline NiAl has been observed by Ball and Smallman to have $\langle 011 \rangle$ $\{100\}$ and $\langle 001 \rangle$ $\{100\}$ operative slip systems [30]. An insufficient number of slip systems is observed in NiAl to satisfy Von Mises criterion for deformation. Dislocations with non $\langle 100 \rangle$ slip vectors may give rise to plasticity in NiAl. At temperatures above DBTT, a combination of glide and

climb of $\langle 100 \rangle$ dislocations may satisfy Von Mises criterion and enhance deformability.

NiAl in the range of 57 at. % Ni to 66 at. % Ni has been shown to exhibit strain induced martensite. This mode of deformation also shows internal twinning in the martensite plates [34].

Fracture of stoichiometric polycrystalline NiAl remains primarily intergranular at room temperature. Transgranular cleavage is observed in the case of stoichiometric polycrystalline NiAl with increasing strain rate [35]. It has also been reported that increasing the stoichiometric deviation of NiAl increases the tendency towards transgranular cleavage at room temperature [30].

Fracture of martensitic NiAl occurs along twin boundaries when the twins are 10-20 μm thick, and occurs along twin and grain boundaries when the twins are finer [36].

2.3 MARTENSITIC TRANSFORMATION

Martensite is a product of a thermoelastic phase transformation. It is a diffusionless or displacive transformation. In this type of transformation a rearrangement of atoms of a finite volume of the parent phase produces a new crystal structure. The realignment of atoms causes a change in shape leading to distortion of the surrounding matrix. The displacement of atoms is small in relation to their neighbours, however lattice correspondence is maintained as shown in Fig.[10].

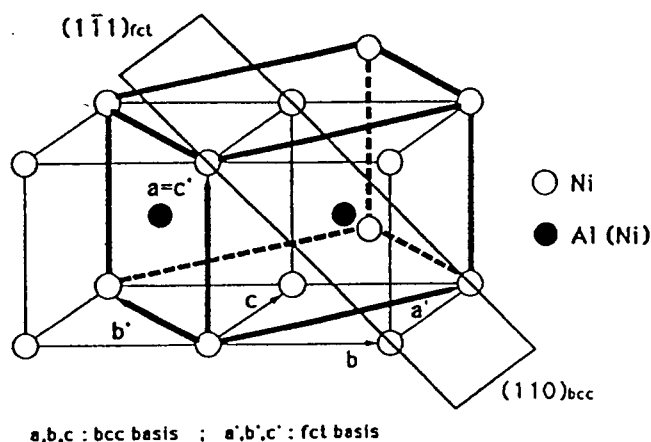


Figure [10] - Lattice correspondence and CsCl structure transformation to fct or CuAuI structure in martensitic transformation-Ref. [54]

There is no compositional change as the parent structure (austenite) [37] changes to the product phase (martensite). The martensite is usually observed as platelets or plates in the micro-structure.

The plane on which the martensite forms is assumed to be an undistorted plane. This is termed the "habit" plane. Due to the formation of the martensite phase, a shear component occurs parallel to the habit plane and a tensile or compressive strain perpendicular to the habit plane. This strain is termed the "invariant plane

strain". Three basic deformation mechanisms are required for the martensitic transformation [38] to occur. These are:

1. Bain distortion: Forms product lattice from parent lattice.
2. A shear deformation: To maintain lattice symmetry in order to produce an undistorted or "habit" plane.
3. A rotation of transformed lattice: This maintains orientation of the habit plane in both the parent and the transformed phase.

The above three deformation mechanisms may occur in any random manner but will satisfy conditions for the martensite reaction to be completed. The lattice correspondence is met by the Bain distortion. The shear deformation occurs either through internally slipped or internally twinned martensite [39] as shown in Fig. [11].

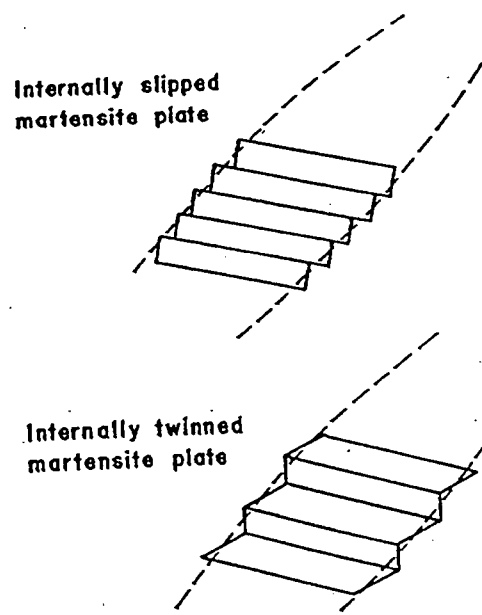


Figure [11] - Shear deformation by slip or twinned substructure in martensite variant - Ref. [40]

When the martensitic reaction is caused by thermal changes, it is termed "thermal" martensite. However, when it occurs at a constant temperature it is called "athermal" transformation. The temperatures corresponding to the start and finish of the martensite reaction are termed M_s and M_f respectively. If plastic deformation has occurred prior to M_s temperature being reached, the highest temperature at which martensite forms is designated M_d . The corresponding austenite start temperature for plastic deformation is termed A_s . The reverse transformation i.e. the temperature for martensite to be fully transformed into austenite upon heating is termed the A_f temperature. These are shown in Fig. [12].

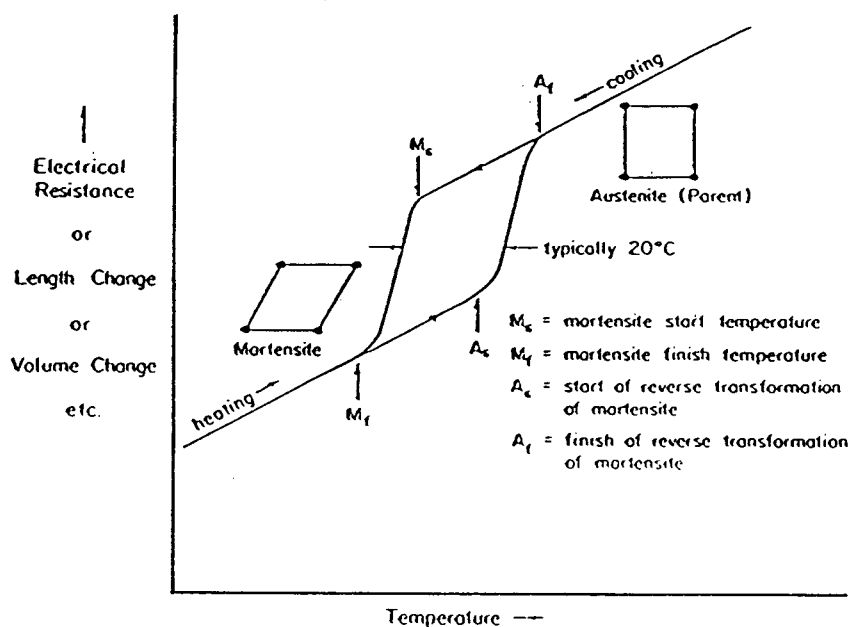


Figure [12] - A_s and A_f temperatures for martensitic transformation - Ref.[51]

The martensite reaction also occurs due to application of stress. Applied stress can either raise or lower the M_s temperature depending on the direction of the stress component. Single crystal Au 47.5% at. % Cd alloy, due to a low invariant plane strain component, shows a transformation front which passes across the crystal since the strain is lowered as the temperature is lowered in the alloy. This is shown in Fig. [13].

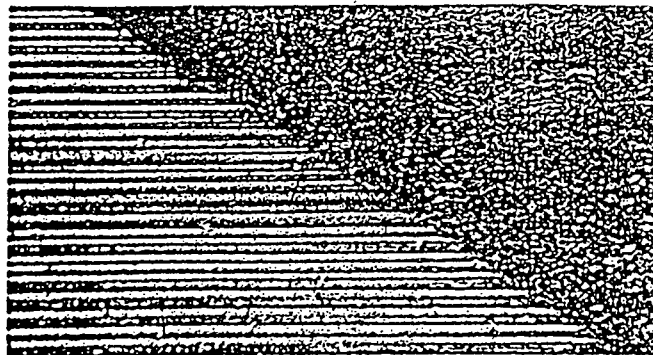


Figure [13] - Au 47.5 at. % Cd alloy showing transformation front - Ref. [39]

NiAl undergoes a martensitic transformation both in the quenched and deformed samples [34]. In Ni-rich NiAl, the ordered austenite phase with the CsCl or bcc structure can transform martensitically to a CuAuI or face centred tetragonal (fct) structure [41] as shown in Fig. [10]. Since the excess Ni atoms are accommodated by substitution on the Al(001) fct planes, the composition of NiAl will have a direct influence on the tetragonality of the martensite phase.

The substructure of the martensite consists of internal twinning on the $\{111\}\langle 112 \rangle_{\text{fcc}}$ system [42]. The deformation of martensite below the M_f temperature occurs by detwinning of internal twins [42]. Fig. [14] shows that this twin density decreases with an increase in the nickel content [41].

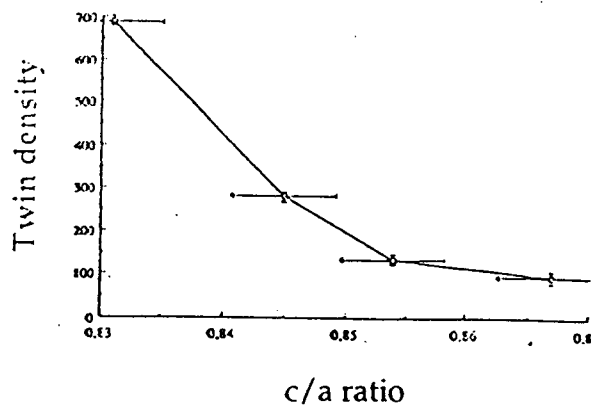


Figure [14] - Twin density variation with nickel content in NiAl - Ref. [41]

2.3.1 SHAPE MEMORY EFFECT

When the austenite phase transforms to a martensite phase, numerous plate orientations having a single martensitic crystal structure result from a given orientation of the austenite. The need for many orientations of martensite arises in order to satisfy imposed boundary conditions. These martensite orientations remain coherent with respect to austenite and free of internal stress [37] due to self accommodation.

The shape memory effect (SME) is the ability of the material to remember its previous shape above a critical temperature even though it might have undergone deformation at a lower temperature. Fig. [15] shows how shape memory effect works for materials which exhibit martensitic transformations. From Fig. [15] it is seen that on cooling the higher temperature austenite

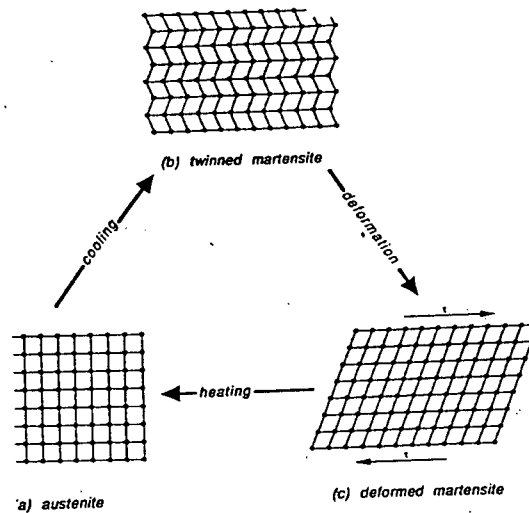


Figure [15] - Shape memory effect in martensitic transformations - Ref. [44]

temperature austenite phase transforms to martensite as in (b). There is no change in shape at this stage because of self accommodation. However, if deformed by external stress below the M_f temperature, it forms a new

microstructure as indicated in (c) of the Fig. [15]. Now if the temperature is raised, the specimen will go back to its original shape which is indicated in (a).

During the martensite formation, the shear deformation can be achieved either by internal slip or internal twinning mechanism. However slip is an irreversible process whereas twinning is a reversible [44] process of accommodation. Therefore, for shape memory to occur, the deformation of the martensite must take place through twinning as opposed to slip. Fig. [15]- (c) shows that the deformed martensite on heating to above A_f temperature will revert back to its austenite structure. In the example discussed above the formation of martensite has come about due to a change in temperature. However, a martensite transformation can also be brought about through an application of stress in place of a change in temperature.

Since martensite transformation is a thermoelastic process, there is an equivalence between temperature and stress i.e. a decrease in temperature is equivalent to an increase in stress, with both stages stabilizing martensite. Martensite can form at temperatures above M_s on application of stress and the martensite so formed is called stress induced martensite (SIM). The driving force is now mechanical rather than thermal in nature. As the M_s temperature is approached, the stress required to form SIM is reduced, as shown for the intermetallic Cu-Zu in Fig. [16].

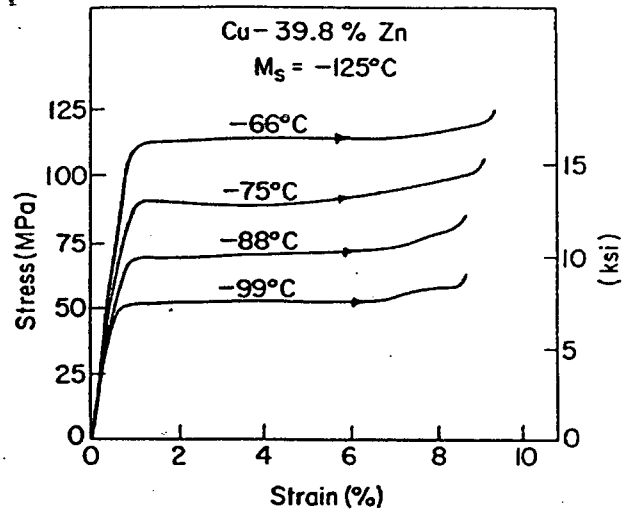


Figure [16] - Stress-strain curve for Cu-Zn showing reduced stress required as M_S temperature is approached - Ref. [51]

The equivalence of stress and temperature in a martensitic reaction is depicted by the Clausius-Clapeyron equation:

$$d\sigma/dM_S = -\Delta H/T\varepsilon_0 \dots\dots\dots(1)$$

where

- T: Temperature
- ΔH : Transformation latent heat
- σ : Applied stress
- ε_0 : Transformational strain resolved along direction of the applied stress

Fig. [17] shows that the linear relationship of this equation is followed in the case of Cu-Zn alloys. The temperature range for SIM is from M_S to M_d .

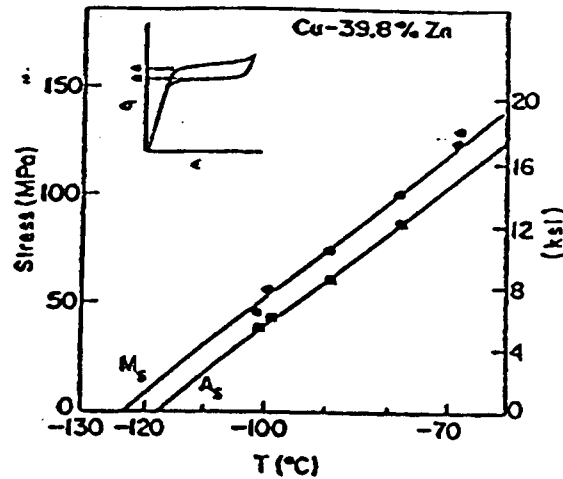


Figure [17] - Linear relationship of the Clausius-Clapeyron equation in case of Cu-Zn alloy - Ref. [51]

Superelasticity (SE) occurs when a material is deformed by applying stress at a temperature above A_s but still below M_d . When the stress is removed the strain is fully recovered.

NiTi which has a B2 structure is known to exhibit good sliding contact wear behaviour [45]. This is due to SME. The process of SME is due to an intermediate rhombihedral(R) phase transformation. The contact area increases due to the SME leading to a reduced local stress. Strain rate (ϵ) also affects the martensite transformation (MT) stress [46]. For $\epsilon < 10\%/min$, the transformation stress remains independent of ϵ in NiTi. However for $\epsilon \geq 10\%/min$, the martensite transformation stress increases and the reverse transformation stress decreases with an increase in ϵ .

For NiAl to show SME there are certain prerequisites:

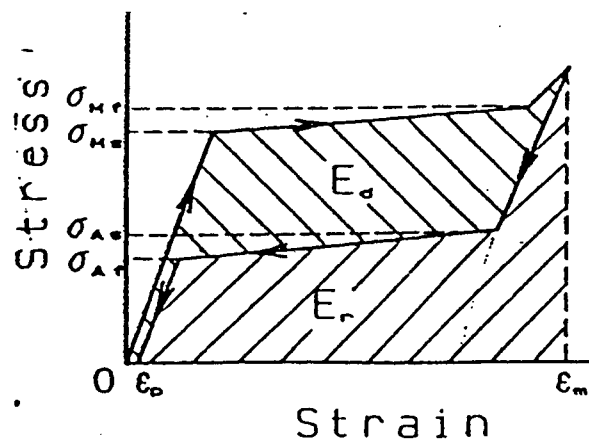
1. The martensite transformation must be thermoelastic.
2. The martensite phase must remain ordered as does the austenite phase.
3. The martensite must be capable of twinning.

NiAl in fact exhibits SIM transformation above M_S temperature and shows SME. The shape recovery begins at the A_S temperature and ends at A_f temperature [43]. The mechanism of shape recovery is due to detwinning i.e. a stress induced alteration of the twin ratio in each variant.

2.3.2 STRAIN INDUCED TRANSFORMATION

It has been noted earlier that in alloys that exhibit SME, the martensite does not revert back to austenite as a result of removal of stress alone. It will only revert to the austenite phase on reheating the alloy.

If the martensite reverts back to its parent phase on removal of external stress, i.e. it recovers all the strain, it is said to exhibit superelasticity (SE) or pseudoelasticity (PE). Fig. [18] shows the stress-strain diagram for materials exhibiting SE.



E_d : dissipated strain energy density per unit volume

E_r : recoverable strain energy density per unit volume

Figure [18] - Stress-strain diagram for materials showing SE - Ref. [46]

The formation of martensite involves both the shear and normal components of strain. Hence as the strain increases, the nucleation of martensite is made easier [38]. Also the increased strain in the martensite will require a lower stress for the martensite to revert back to its austenite phase. Thus strain will bring the forward and reverse transformation paths closer

thereby giving a better SE. The total deformation strain, if it goes beyond a certain limit will however, lead to plastic behaviour or slip activation. The recoverable transformation strains are not dependent on the strain recovery modes [48]. The transformation strains are found to depend on crystal orientation [49]. Since transformation strains depend on crystal orientation, the magnitude and direction of the martensite shape strain is important. Wayman and Chakravorty have shown that there is no isotropic distortion of the martensite and the parent phase interface [50], hence the martensite obtained in NiAl is thermoelastic. The schematic representation to analyze this is shown in Fig. [19].

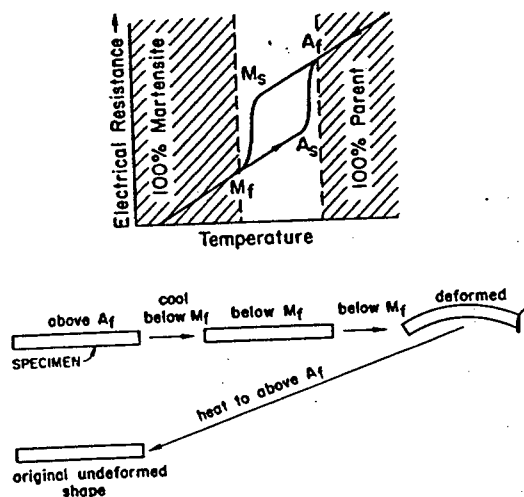


Figure [19] - Schematic representaton for thermoelastic nature of martensite formed in NiAl - Ref. [44]

NiTi alloys show a change in microstructure as the tensile strain increases. At 5% strain there is a transformation from β to R phase and as the strain reaches 10%, the $R \rightarrow M$ reaction occurs.

As there is a gradual build up of strain, the time for the incubation of martensite nuclei will increase [51]. Although this is for thermal martensite,

the morphologies of both thermal and isothermal martensites are found to be similar, hence the time dependence with incubation should also hold for both the martensites .

In NiAl there is a "hard" and "soft" orientation as mentioned in Section 2.2 and therefore crystal orientation should play a significant role in the accumulation of strain in a particular orientation. This is illustrated in Fig. [20].

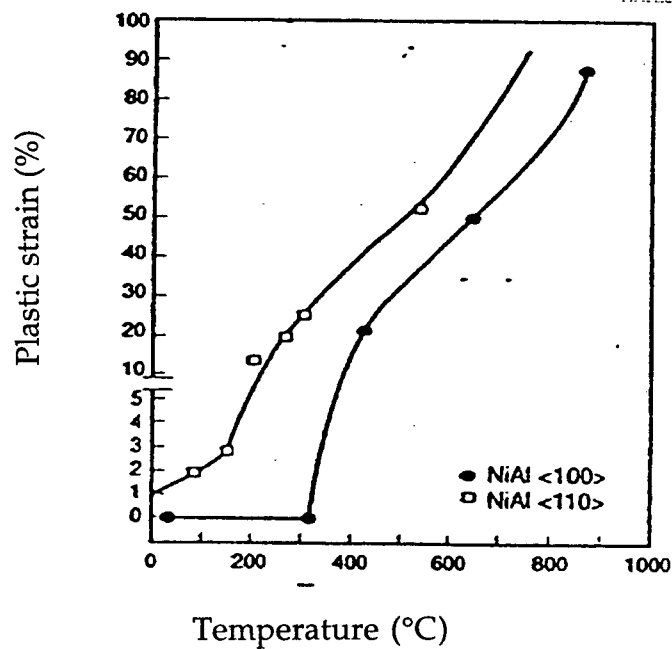


Figure [20] - Crystal orientation effect for stoichiometric NiAl - Ref. [13]

As the strain will be different in different orientations, the percentage of martensite in a particular orientation obtained will depend on the crystal orientation of the grain.

Strain induced martensite in NiAl is found to develop a twinned structure which if the strain increases will deform to accommodate this increased strain.

SE can be improved by:

1. Increasing austenite phase strength as this will increase the M_d temperature [52].
2. Decreasing the strain rate as this will also raise the M_d temperature.

2.3.3 DEFORMATION OF STRAIN INDUCED MARTENSITE

NiAl in the composition range of 57 at. % Ni - 66 at. % Ni is found to show stress induced martensite transformation [34]. This martensite has a LL_0 or CuAuI structure and a substructure which is internally twinned [53]. The internal twinning is on a $\{111\} \langle 112 \rangle$ fct system [54].

In hcp cobalt single crystals high cavitation erosion resistance has been found to be associated with twinning [55]. There is an increase in the cavitation resistance as the twin density increases and also as the inter-twin spacing decreases. This is due to an increased resistance to fatigue crack propagation.

Ball [34] in 1967 reported that a NiAl 57 at. % Ni crystal when compressed along $\langle 100 \rangle$ at a high strain rate of 10^{-2} sec^{-1} showed colonies of martensite. Fracture was observed at a stress of 1034 MPa (150×10^3 psi) with little or no plastic deformation. The fracture was simultaneous to the occurrence of martensite in the material.

A strain rate increase in NiTi alloy is found to increase the dissipated strain energy Fig.[18]. This increases the material's capacity to absorb shock. However, it also leads to faster fatigue damage [46]. Work hardening in NiTi is found to limit the mobility of the martensite transformation interface [56]. When NiAl crystals, with LL_0 (3R) martensite having internally twinned substructure, are deformed in tension, a different substructure is obtained depending on crystal orientation. When stress is applied along $\langle 100 \rangle$

the martensite variant becomes a single crystal with no internally twinned substructure and exhibits 13% elongation [57]. However in the $\langle 011 \rangle$ orientation, it becomes twinned with a single twin system. NiAl $L1_0$ (3R) martensite under compression has been reported by Kim and Wayman, to deform by detwinning of the martensite substructure [58]. Hence detwinning of internal twins of $L1_0$ (3R) martensite in NiAl alloys is the essential mechanism of deformation both in tension and compression.

The presence of {111} stacking faults are also reported in NiAl $L1_0$ (3R) martensite [42]. Deformation by slip with a reduction in the separation of the superpartial dislocation can also be expected.

Deformation of SIM in NiAl will thus be controlled by a shear mechanism and will depend on the shear level reached. Detwinning induces an additional strain [59] which can be expressed as :

$$\text{Strain} = (S) \times O_f \times V_\tau \dots\dots\dots 2$$

- where
- S = magnitude of the twinning shear
 - O_f = Schmidt factor or Orientation factor
 - V_τ = Volume ratio of the detwinning part

The maximum strain has been estimated at 0.07 - 0.13.

3.0 EXPERIMENTAL WORK

Ni_3Al :

This alloy was melted from 99.9% purity Aluminum ingot and 99.99% purity nickel plate. Melting was carried out using induction heating in an alumina crucible under an argon gas atmosphere. A graphite mold with a riser cavity was used. The entire mold assembly was preheated to 600°C and placed on a 4" x 4"x10" copper chill block as shown in the Fig.[21]. The pouring temperature was approximately 1500°C .

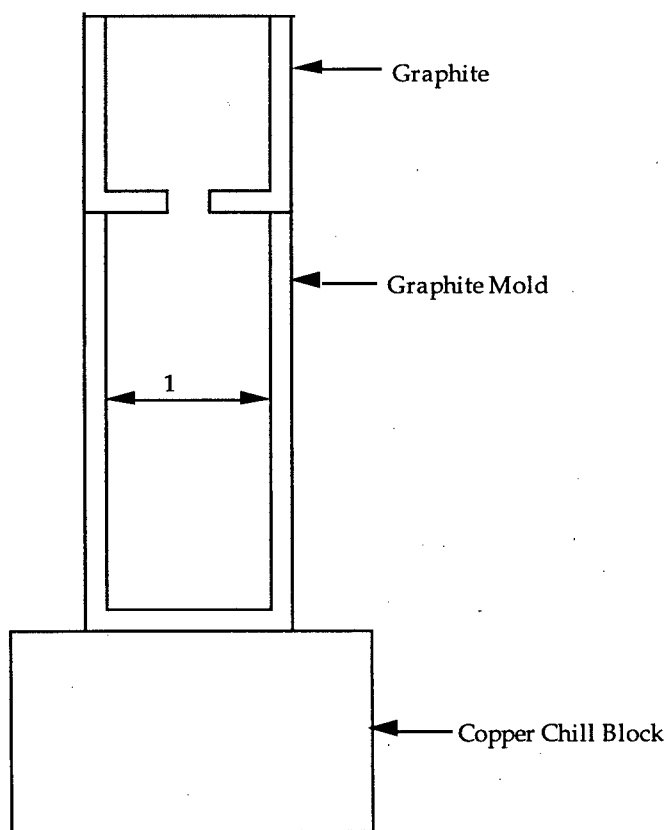


Figure [21] - Schematic casting set up for Ni_3Al bar casting

The riser was cut off and the 1" diameter bar surface was milled to a depth of

1/8" from the surface. Hardness readings were taken at periodic intervals of 1/2" along the 8" length of the bar, these are shown in Fig. [22]. Since a variation in hardness indicated segregation to have occurred, the bar was then

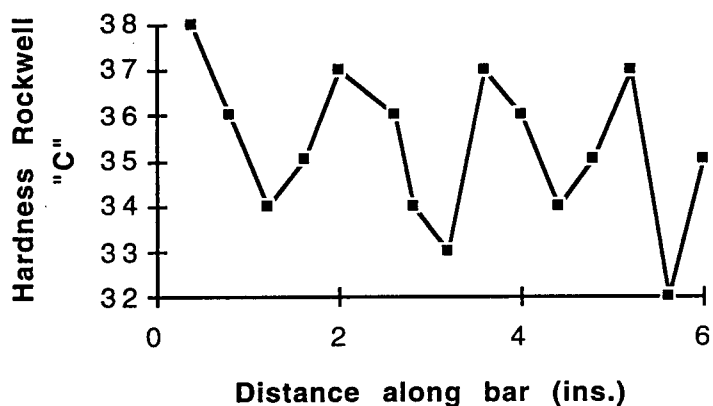


Figure [22] - Hardness readings for Ni₃Al along the bar length

given a homogenization annealing cycle. The cycle followed was 192 hours at 1000°C followed by 48 hours at 800°C and 2 hours at 600°C with cooling to room temperature. Energy Dispersive X-ray Analysis (EDXA) was done of the bar and the results are shown in Fig. [23].



Figure [23] - EDXA results for Ni₃Al bar

The hardness readings taken after annealing are shown in Fig. [24].

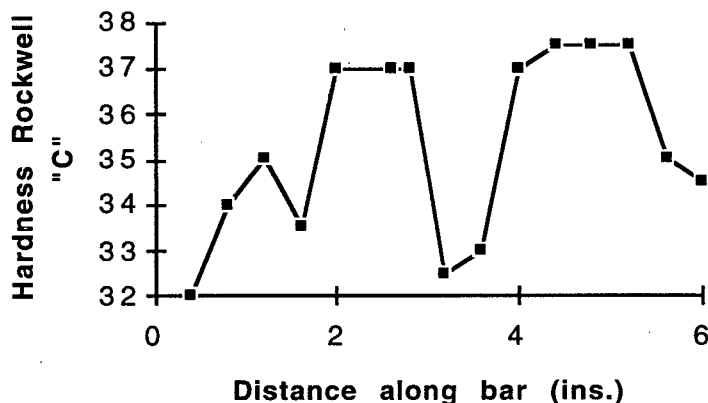


Figure [24] - Hardness readings after homogenization anneal for Ni_3Al

Since inhomogeneity existed even after annealing, the bar was sliced by a silicon-carbide wheel at the point where the EDXA showed a stoichiometric composition of Ni_3Al . The 0.75" thick sample was milled and polished to a 600 grit surface finish. Cracking was observed on one surface of the Ni_3Al sample. Cavitation erosion tests were carried out on the cracked and the uncracked surfaces using a modification of ASTM G-32-92 "Standard Test Method for Cavitation Erosion Using Vibratory Apparatus"[62]. In the standard test the specimen is vibrated whereas during the modified test the specimen was kept stationary and a cavitation zone was created using a vibrating horn tip. Some tests were conducted using the standard amplitude of $\pm 25 \mu\text{m}$, others were carried out at a lower amplitude $\pm 16 \mu\text{m}$ to examine the influence of the cavitation intensity (amplitude). Likewise, surface finish was kept as per ASTM standard for some tests while others were conducted with different types of surface finish. The tests were carried out only a single time on each specimen in the present work. Due to the close limits

on the test conditions the erosion rate should not vary more than $\pm 5\%$ [68].

A schematic of the cavitation test apparatus used is shown in Fig. [25]. It consists of a transducer horn which oscillates with a frequency of 20 KHz as

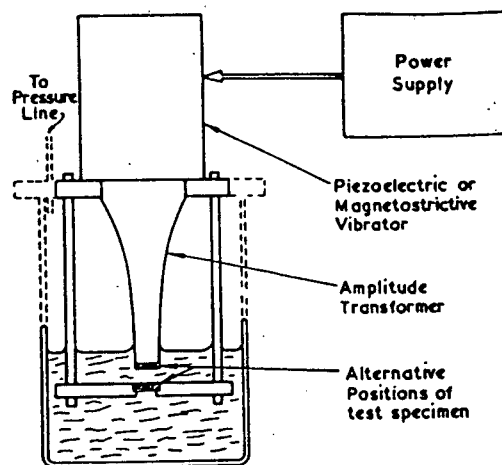


Figure [25] - Schematic of the cavitation test apparatus - Ref. [2]

per ASTM G-32 standard. The amplitude can be varied by means of a controller. The sample to be tested can be threaded into the horn tip if it is ductile and machineable. In case of brittle materials, the sample is held stationary in a fixture. The vibrating tip was made up of a cavitation erosion resistant Stellite alloy. A distance of 0.5 mm was maintained between the oscillating tip and the top surface of the fixed sample. The oscillating tip sample had an area of 1 square cm. and the weight range of 10.000 - 10.400 g. maximum as per ASTM G-32. A portion of the horn along with the tip and the fixed sample is immersed into a beaker of distilled water. The water

temperature was controlled to $20^{\circ}\text{C} \pm 1^{\circ}\text{C}$ by means of cooling coils connected to a thermostatic controller. (The standard specified $25 \pm 2^{\circ}\text{C}$).

The sample was polished and mounted in the fixture. At intervals during the test, the sample was removed, washed in alcohol, dried and weighed on an electronic Mettler H 80 balance with 0.0001 g. accuracy and a maximum sample weight capacity of 160 g. Mass loss measurements were recorded at regular time intervals. The total test time was variable being as long as 30 hours for a single specimen.

NiAl:

Certain difficulties, such as microporosity and carbon diffusion, were experienced during the casting of Ni_3Al . In order to circumvent these difficulties it was decided to obtain NiAl samples from other sources. Oak Ridge National Laboratories (ORNL) has been producing NiAl on a regular basis. It was, therefore, decided to procure the bars with a cross section of 0.5" x 1" from ORNL. The bars are shown in Fig. [26]. These samples were arc-melted in vacuum and drop cast into a water cooled copper mold. The compositional analysis shown in Table [IV] was done at Cantest Laboratories, Vancouver, Canada. The method of analysis was Plasma Spectroscopy with a detection limit of 0.01% on each element.

Samples were cut by an electric discharge machine (EDM), ground, polished and tested for cavitation erosion in accordance with the modified ASTM G32-92 specification. The amplitude of the vibrating horn and the surface finish

of the samples were modified to study their response to cavitation erosion.

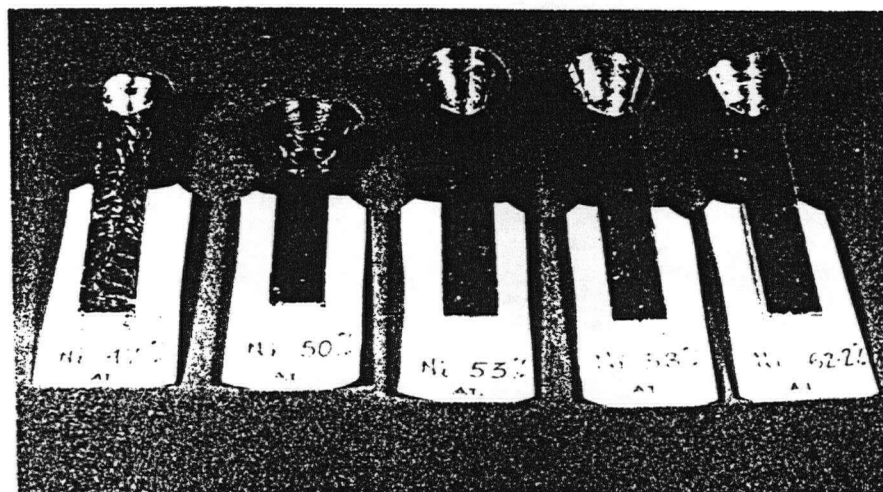


Figure [26] - NiAl bars procured from Oak Ridge National Laboratories with different nickel percentages

Table IV - Compositional Analysis of Test Samples

NOMINAL COMPOSITION	At. Wt.	48	50	53	58	62.2
% Ni		66	69	71	75	78
Aluminum	Al	34.3	29.3	28.6	24.8	21.5
Antimony	Sb	< 0.15	< 0.15	< 0.15	< 0.15	< 0.15
Cadmium	Cd	< 0.03	< 0.03	< 0.03	< 0.03	< 0.03
Chromium	Cr	< 0.03	< 0.03	< 0.03	< 0.03	< 0.03
Cobalt	Co	< 0.02	< 0.02	< 0.02	< 0.02	< 0.02
Copper	Cu	0.27	0.03	0.10	0.04	0.08
Iron	Fe	0.08	0.09	0.04	0.09	0.15
Lead	Pb	< 0.08	< 0.08	< 0.08	< 0.08	< 0.08
Magnesium	Mg	<	<	<	<	<
Manganese	Mn	<	<	<	<	<
Molybdenum	Mo	< 0.04	< 0.04	< 0.04	< 0.04	< 0.11
Nickel	Ni	65. (a)	71. (a)	71. (a)	75. (a)	77. (a)
Tin	Sn	< 0.03	< 0.03	< 0.03	< 0.03	< 0.57
Vanadium	V	<	<	<	<	<
Zinc	Zn	0.03	0.02	0.45	0.07	0.29

Results expressed as percent (%)

< = Less than detection limit

(a) = Result calculated by difference. For better precision at high level, a classical analysis is recommended.

General:

Optical and scanning electron microscopy (SEM) were used as aids to the interpretation of results on cavitation erosion. The SEM studies were performed on a Hitachi Model S-2500 microscope. Some of the NiAl samples were analyzed by X-ray diffraction (XRD) method on a Philips X-ray Diffractometer using a copper target with a nickel filter. The Cu-K α wavelength was used for diffraction studies. The accelerating voltage and current were 36KV and 20mA., respectively. The scan speed used was 1°C per minute and the slits used were 2°/0.2°/2°.

4.0 RESULTS AND OBSERVATIONS

Ni₃Al:

The microstructure of the cast bar showed directional solidification towards the centre and elongated (columnar) grains. Graphite particles were observed dispersed in the metallic matrix, coming likely from the mold. The carbon was in a spheroidized form as shown in Fig. [27]. The XRDA as shown in Fig.

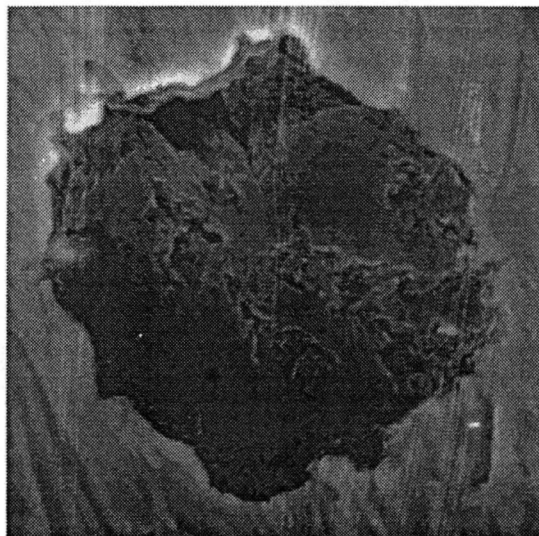


Figure [27] - SEM photograph of spheroidized carbon in Ni₃Al bar (34,00X)

[28] confirmed the composition of the carbon nodule.

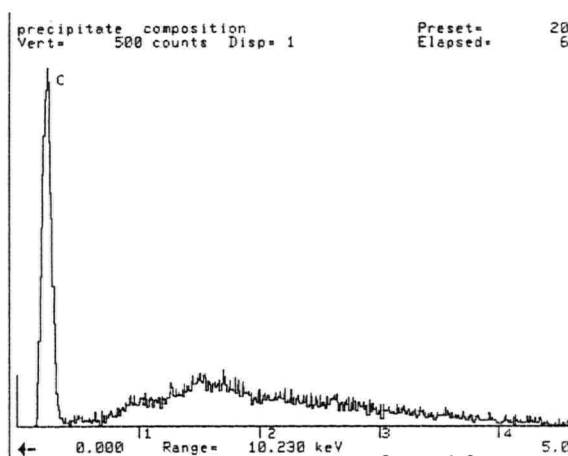


Figure [28] - EDX pattern of carbon nodule

Ni₃Al cracked sample:

A crack was observed on the sample surface before the cavitation erosion test was conducted. On subjecting to cavitation erosion testing, within half an hour the sample showed radial cracks starting at the centre. These cracks increased in length as the testing time increased. Cavitation erosion was observed to initiate at the cracks. The cracks appeared to be along definite macroscopic planes as seen in Fig. [29]. This indicated the brittle nature of the material.

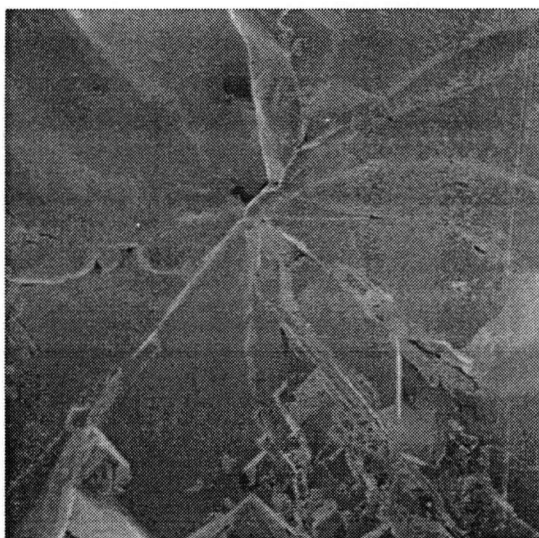


Figure [29] - SEM photograph of cracks in Ni₃Al sample (20X)

The cavitation erosion test results are shown in Fig. [30] in which cumulative or total mass loss is plotted against test time. The test was carried out with a sample surface finish of 600 grit and test amplitude $\pm 16 \mu\text{m}$.

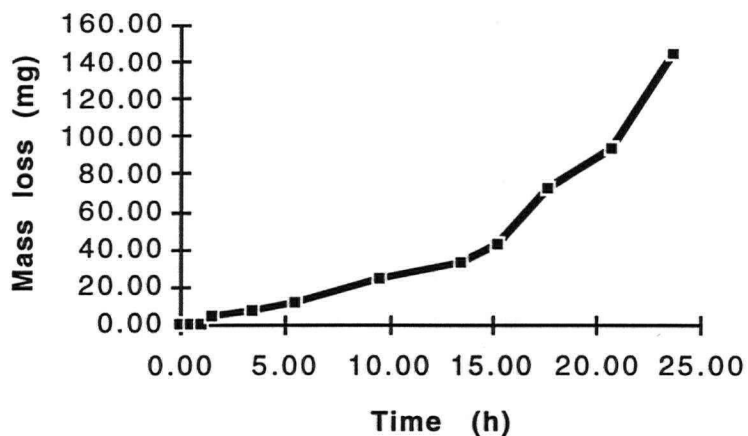


Figure [30] - Cavitation mass loss curve of Ni₃Al (cracked sample)

Although radial cracks were observed in the first half hour of testing, there was no mass loss for one hour. Hence the energy released by the bubble implosion was absorbed in crack initiation and propagation. From Fig. [31] it is seen that there are certain regions where no erosion was observed after 24 hours of testing.

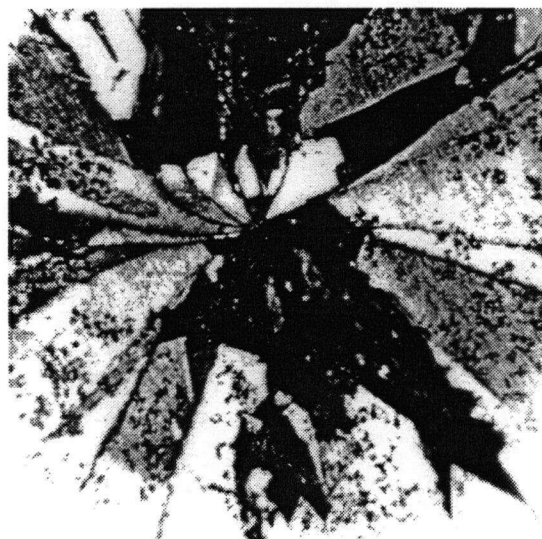


Figure [31] - Ni₃Al (cracked) sample after 24 hours of testing (50X)

The microstructure of these regions is shown in Fig. [32]. The appearance is

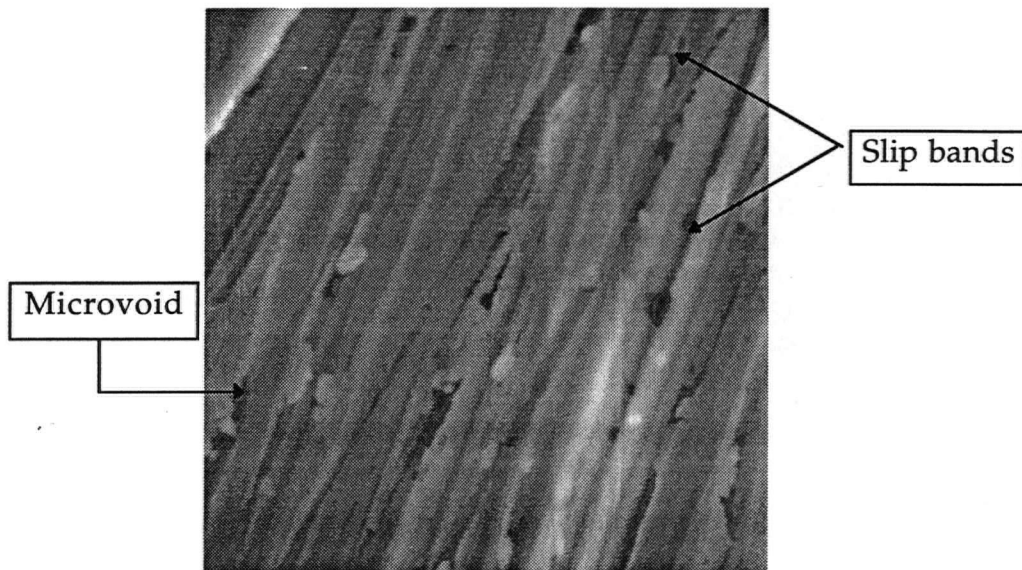


Figure [32] - SEM photograph of persistent slip bands with microvoids in Ni₃Al (cracked) sample after 24 hours of cavitation testing (5.00 K)

similar to the persistent slip bands with microvoids observed by Stoloff [25] during the plastic deformation studies of Ni₃Al polycrystals. The microvoids would eventually coalesce and initiate cracks, leading to fracture and mass loss. A mass loss rate of 4.8 mg/h due to cavitation erosion was observed in the cracked Ni₃Al sample.

Ni₃Al uncracked sample:

The result of the cavitation test is shown in Fig. [33]. The test was carried out with a sample surface finish of 600 μm and a test amplitude of $\pm 16 \mu\text{m}$.

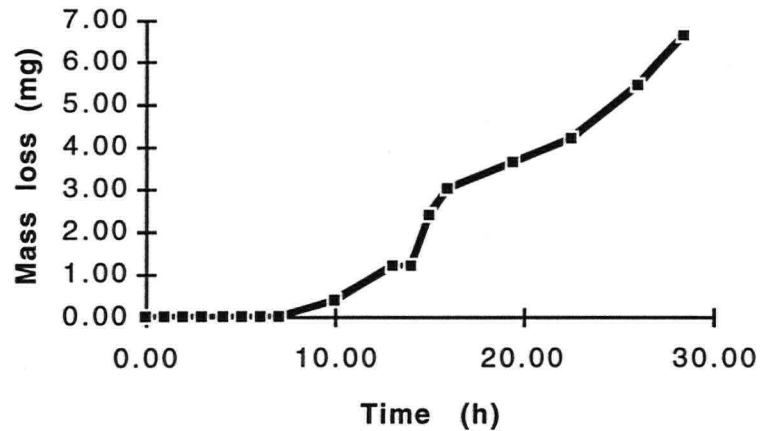


Figure [33] - Cavitation mass loss curve for Ni_3Al (uncracked sample)

This shows a definite incubation period of 9 hours indicating a fatigue type failure [60] mechanism in Ni_3Al . Fatigue striations were seen on the fracture faces caused by cavitation erosion as shown in Fig. [34]. Cavities were found initiating at microvoids, microporosity, inclusions or other defects. Such locations would be the expected stress raiser locations. Mass loss possibly results from the loss of material connecting two adjacent cavities.

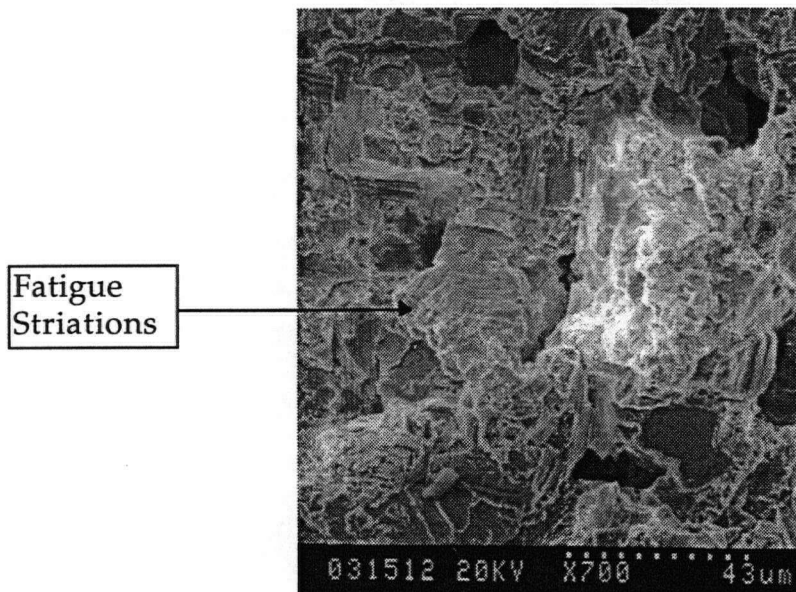


Figure [34] - SEM photograph showing fatigue striations in Ni_3Al during cavitation erosion

No cavitation erosion was observed after 24 hours in the central region of the sample. Fig. [35] shows the SEM photograph of this region. The grains show

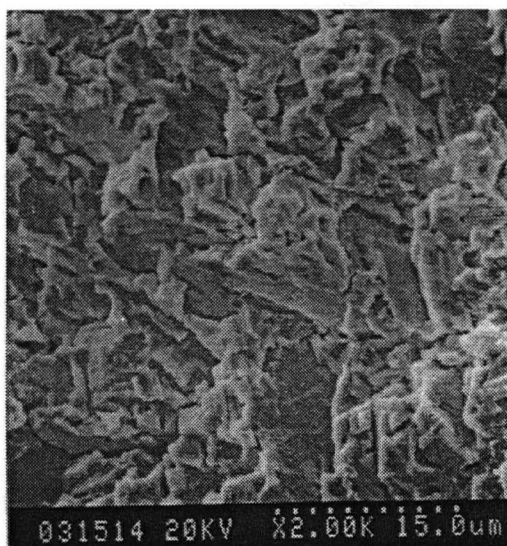


Figure [35] - SEM photograph of Ni₃Al (uncracked sample) after 24 hours of cavitation erosion showing plastic deformation

plastic deformation with no cavitation erosion occurring. No microporosity was observed in this region hence it could be concluded that slip deformation can prevent material loss if the defects such as microporosity are controlled in Ni₃Al. A mass loss rate of 0.4 mg/h was observed due to cavitation erosion in the uncracked Ni₃Al sample.

NiAl:

Five different compositions of NiAl as shown in Table [IV] were tested for their response to cavitation erosion. The following are the results and observation of cavitation erosion tests.

47 at. % Ni:

The microstructure showed equiaxed grains with an average grain size of 620

μm . Because of the brittle nature of this alloy, certain grains on the sample surface had fractured or dislodged during sample preparations. The sample shattered during the Rockwell 'C' hardness testing. Porosity was also observed at triple point junctions of the grains.

The cavitation test results are shown in Fig. [36]. These tests were done at an

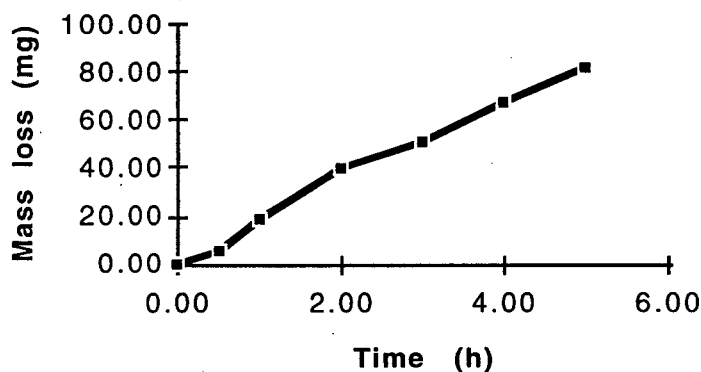


Figure [36] - Cavitation erosion mass loss curve for 47 at. % Ni-NiAl

amplitude of $\pm 16 \mu\text{m}$. There is no incubation period observed and the material loss occurs at a nearly constant rate. The average rate of mass loss is 16.4 mg/h. No plastic deformation or transformation was observed in this alloy.

50 at. % Ni:

The microstructure showed equiaxed grains with an average grain size of $230\mu\text{m}$. Rockwell 'C' hardness readings taken with a diamond indenter showed surrounding grains fracturing along grain boundaries as seen in Fig. [37].

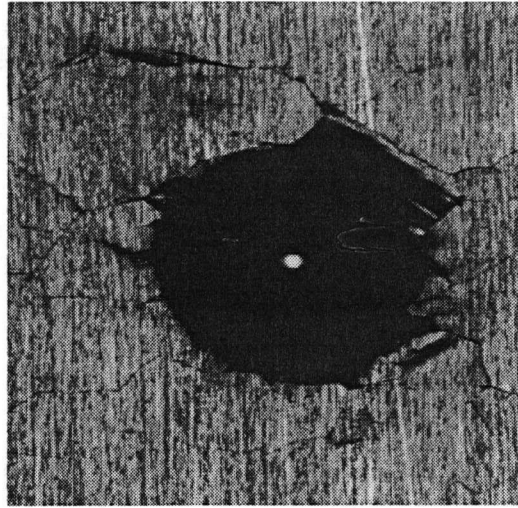


Figure [37] - Grain boundary fracture in 50 at. % Ni seen during Rockwell 'C' hardness testing (50 X)

The SEM photograph in Fig. [38] shows the weak grain boundary cohesion of the of the 50 at. % Ni alloy as seen after impact fracture. Microporosity was observed at triple point junctions.

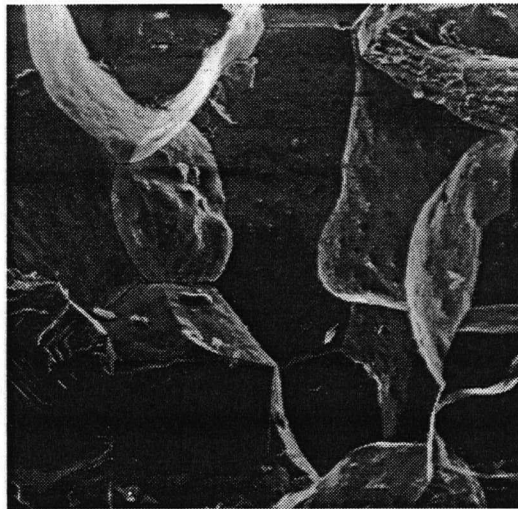


Figure [38] - SEM photograph of 50 at. % Ni fracture surface (200X)

The result of the cavitation testing is shown in Fig. [39] for this alloy. The test was carried out with sample surface finish of 600 grit and a test amplitude of $\pm 16 \mu\text{m}$. The absence of an incubation period can be seen in the graph.

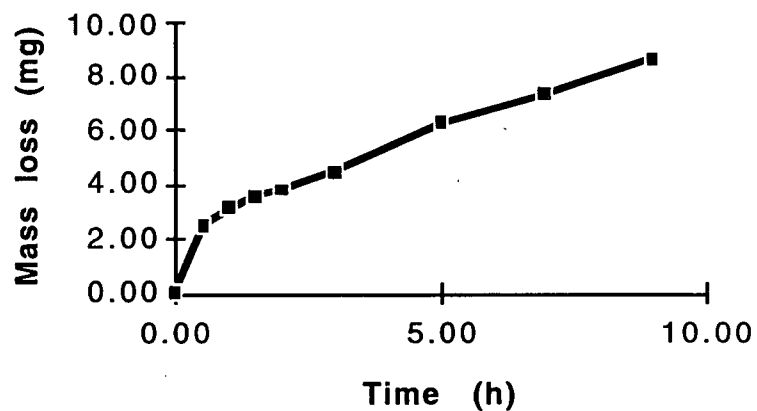


Figure [39] - Cavitation erosion mass loss curve for 50 at. % Ni

Extensive cracking along grain boundaries was seen in the first half hour of the test. The rate of mass loss was 0.7 mg./h. for this alloy. Entire grains were found to be dislodged during the test indicative of the weak grain boundary cohesive strength.

For a better resistance to cavitation erosion, grain boundaries could be strengthened by alloying NiAl 50% at Ni with alloying elements especially those which segregate to the grain boundaries.

53 at. % Ni:

The microstructure of the non-stoichiometric composition showed equiaxed grains with an average grain size of 320 μm . Hardness testing led to cracking at grain boundaries in the vicinity of the indentation. Porosity was observed at grain triple point junctions.

Fig. [40] shows the cavitation erosion test results for the 53 at. % Ni alloy.

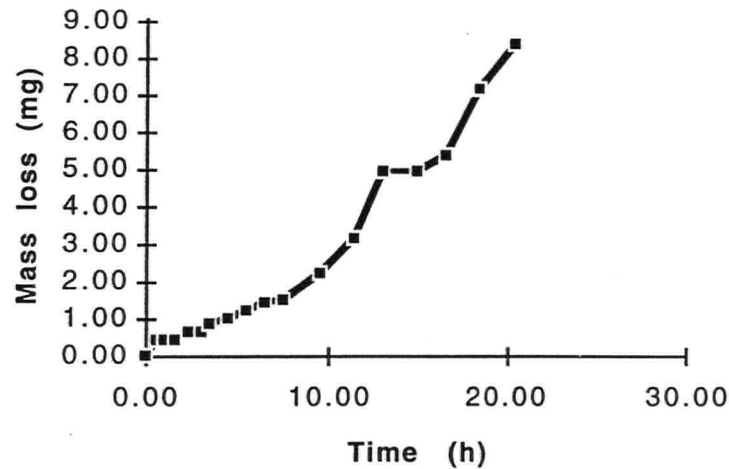


Figure [40] - Cavitation erosion mass loss curve for 53 at. % Ni

Although an incubation period was not observed at the test outset, a short incubation period was observed after one hour. Between 13 - 15 hours total test time, another region of zero mass loss is seen. The average mass loss rate was 0.35 mg/h.

Certain grains were observed not to show any cavitation erosion even after a prolonged period of 20 hours of testing. Fig. [41] shows the microphotographs of a single grain taken at 200 magnification at different

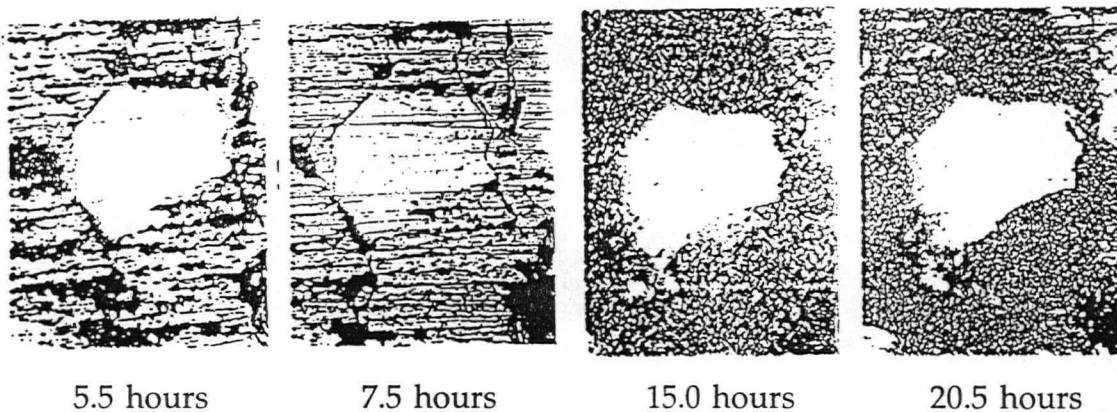


Figure [41] - Single grain of 53 at. % Ni during different stages of cavitation (200X)

time periods during the test. Although the surrounding grains show extensive cavitation erosion after 20.5 hours, the single grain in the centre shows that cavitation is just starting in this grain. The reason for preferential cavitation erosion of grains is not clear at present.

58 at. % Ni:

The microstructure showed equiaxed grains with an average grain size 133 μm . No microporosity was observed at grain triple point junctions. The Rockwell "C" hardness readings when taken did not produce cracking along grain boundaries. The XRDA shown in Fig. [42] is for an uncavitated sample. Presence of thermally induced martensite is indicated by the splitting of

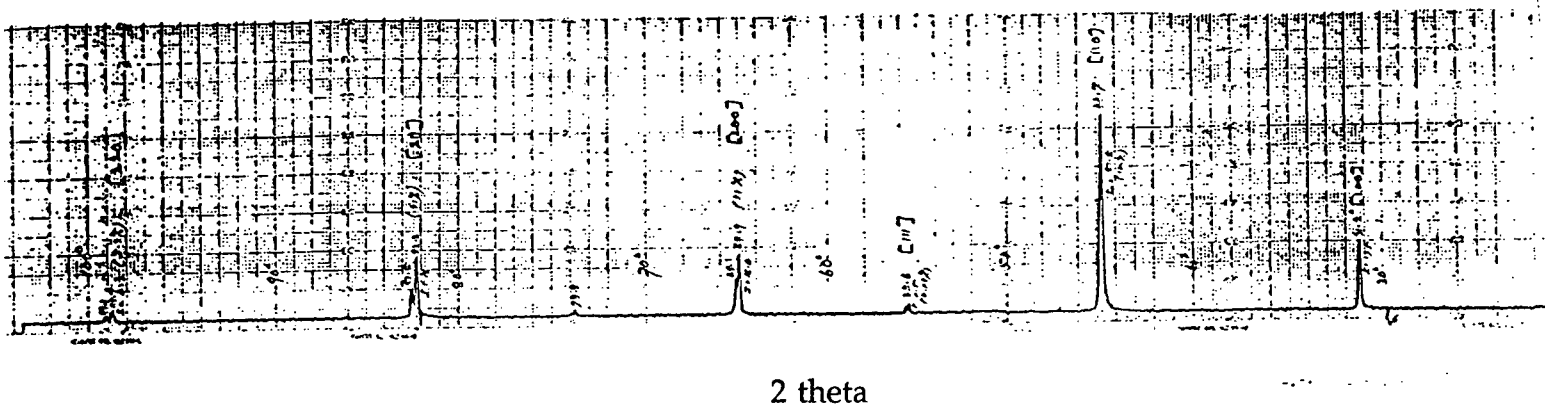


Figure [42] - XRDA graph for 58 at. % Ni uncavitated sample

several reflections at closely spaced angles. Fig. [43] confirms this thermal martensite as seen in the microphotograph of the as cast uncavitated sample of 58 at. % Ni.

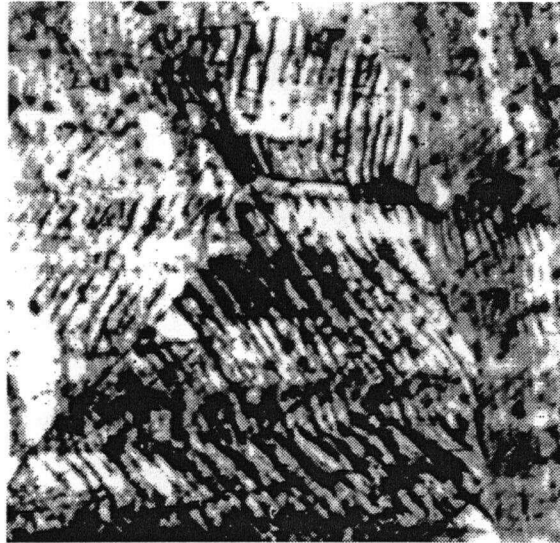


Figure [43] - Microphoto showing presence of thermal martensite in 58 at. % Ni as cast sample in uncavitated condition (500 X)

Fig. [44] shows the cavitation test result of the 58 at. % Ni alloy. The surface finish was 600 grit and the test amplitude was $\pm 16 \mu\text{m}$. The alloy exhibited an incubation period of 5.5 hours. The average rate of mass loss is 0.12 mg./h.

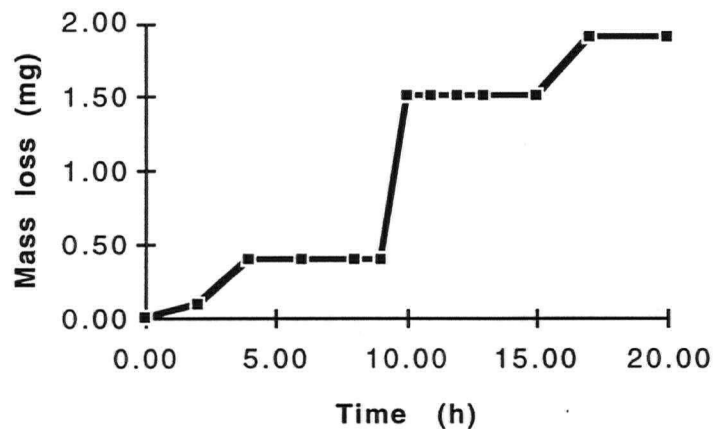


Figure [44] - Cavitation erosion mass loss curve for 58 at. % Ni

The mass loss occurred in a discontinuous manner with time. Alternate periods of no mass loss and mass loss regions may be noted in Fig. [44].

Heymann in a statistical erosion rate model [64] of cavitation erosion confirms that such plateaus of no mass loss can occur, if the distribution function of fatigue had little scatter or dispersion over the surface undergoing cavitation erosion. This would make the lifetime of all the surface elements equal, leading to a step function. In the present work the microstructures observed after several hours of cavitation erosion showed some grains being preferentially eroded in the 53 and 58 at. % Ni compositions. In addition, the 58 at. % Ni composition also shows a strain induced martensite transformation as seen in Fig. [45].



Figure [45] - Strain induced martensite transformation observed during cavitation testing of 58 at. % Ni (1000X)

The steps observed in the erosion curve of Fig. [44] could be due to the transformation occurring. This would lead to absorption of the cavitation bubble energy by the intermetallic compound. The grains which showed no extensive cavitation erosions may be aligned in the 'soft' orientation where extensive plastic deformation is observed as shown in Fig. [46]. Subsequent work hardening of the grain could lead to fatigue fracture and material loss.

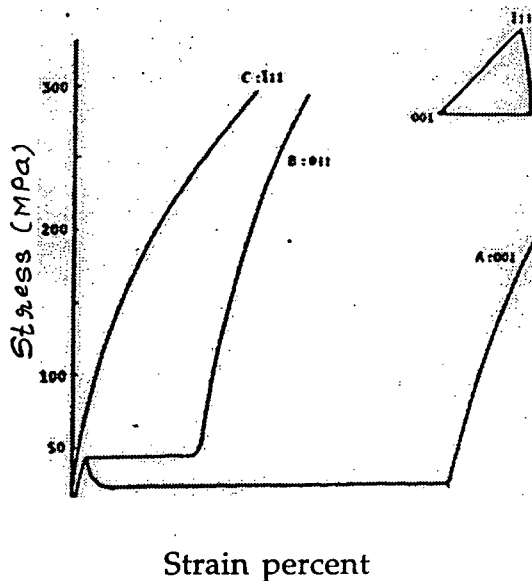


Figure [46] - Graph showing dependence of orientation with strain in NiAl martensite - Ref. [57]

Tests were carried out at a higher amplitude to check the sensitivity of the 58 at. % Ni material to higher intensity cavitation. The cavitation erosion tests conducted at the higher amplitude were as follows:

Amplitude($\pm 25 \mu\text{m}$)/600 grit surface finish - Fig. [47] shows the cavitation test

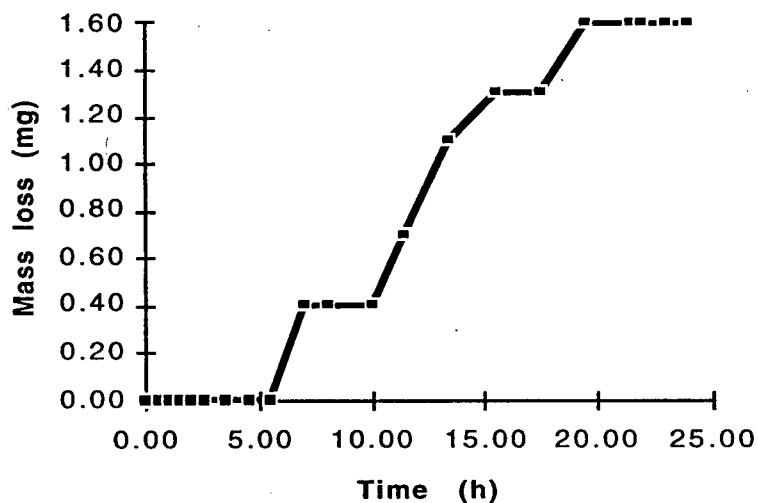


Figure [47] - Cavitation mass loss curve for 58 at. % Ni tested at $\pm 25 \mu\text{m}$ amplitude and 600 grit surface finish

results with these parameters. The incubation period is reduced from to 5.5 hours at an amplitude of $\pm 16 \mu\text{m}$ to 1.5 hours for an amplitude of $\pm 25 \mu\text{m}$, as seen earlier. This indicates that there may be a faster strain accumulation due to the increased test amplitude. The average mass loss rate is 0.12 mg/h. This rate is comparable to the mass loss rate found with $\pm 16 \mu\text{m}$ amplitude and 600 grit surface finish condition for the 58 at. % Ni composition.

The influence of surface finish was also investigated for this composition. Instead of 600 grit finish, a finer finish with $0.05 \mu\text{m}$ alumina was used. The amplitude was $\pm 25 \mu\text{m}$. The results are shown in Fig. [48].

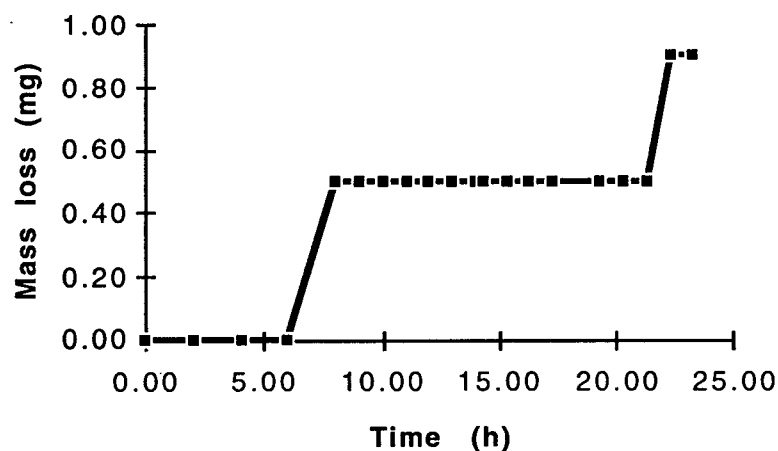


Figure [48] - Cavitation mass loss curve for 58 at. % Ni tested at $\pm 25 \mu\text{m}$ amplitude and $0.05 \mu\text{m}$ surface finish

The average mass loss rate is 0.05 mg./h. The mass loss rate figure is roughly one half of that observed with the 600 grit finish and involving the same amplitude of $\pm 25 \mu\text{m}$. The incubation period has increased to 6 hours from 1.5 hours due to the finer finish. Similarly, a longer plateau (13 hours compared with 5 hours) is seen after the first mass loss period.

An attempt was made to relate the X-ray diffraction intensities of selected peaks with the observed mass loss with time. The specimen was removed at intervals during the cavitation test and was subjected to X-ray diffraction measurements. The results are shown in Fig. [49]. No conclusive correlation could be drawn between the fluctuations in the relative intensities of the various planes and the cavitation erosion mass loss rate observed.

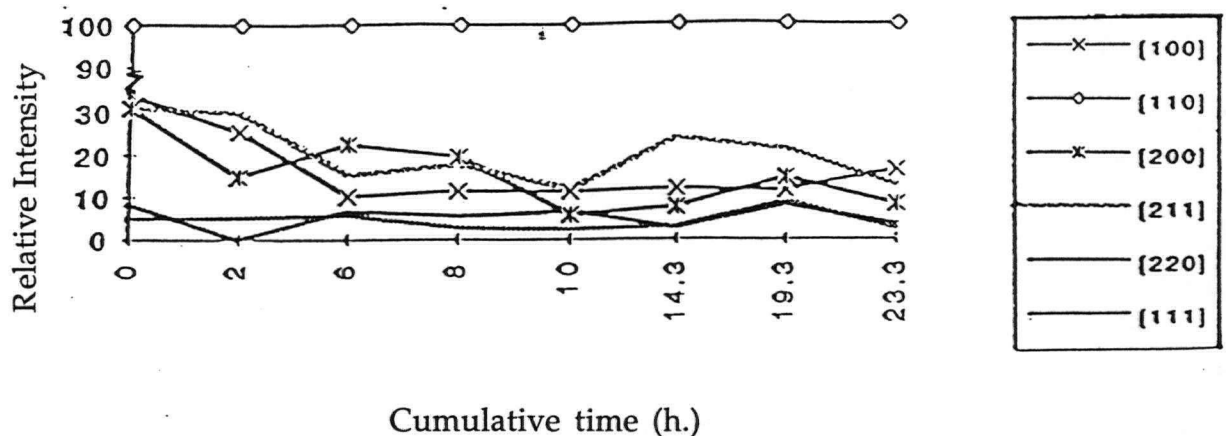


Figure [49] - Variation of intensities of major peaks in 58 at. % Ni during cavitation erosion

Fig. [50] is an optical microphoto of a grain boundary region after 6 hours of

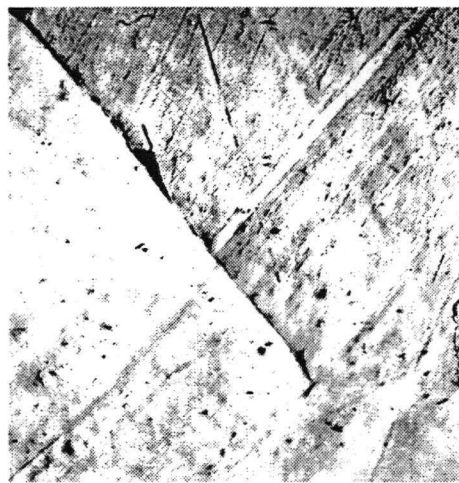


Figure [50] - Optical microphoto of 58 at. % Ni during cavitation erosion testing for 6 hours (1000X)

cavitation testing. The grain on the right hand top shows finer markings which are possibly due to the strain induced martensitic transformation. It indicates strain accumulation which has resulted in grain boundary sliding as evidenced by the shift in the scratch position across the grain boundaries. It also shows erosion beginning at the grain boundary. The grain boundary seems to disappear at the triple point junction at the bottom right of the photo. This could be possibly due to the coherent interface of the intermetallic NiAl at the grain boundary.

Fig. [51](a) shows micro cracks occurring in a geometric pattern after 10 hours

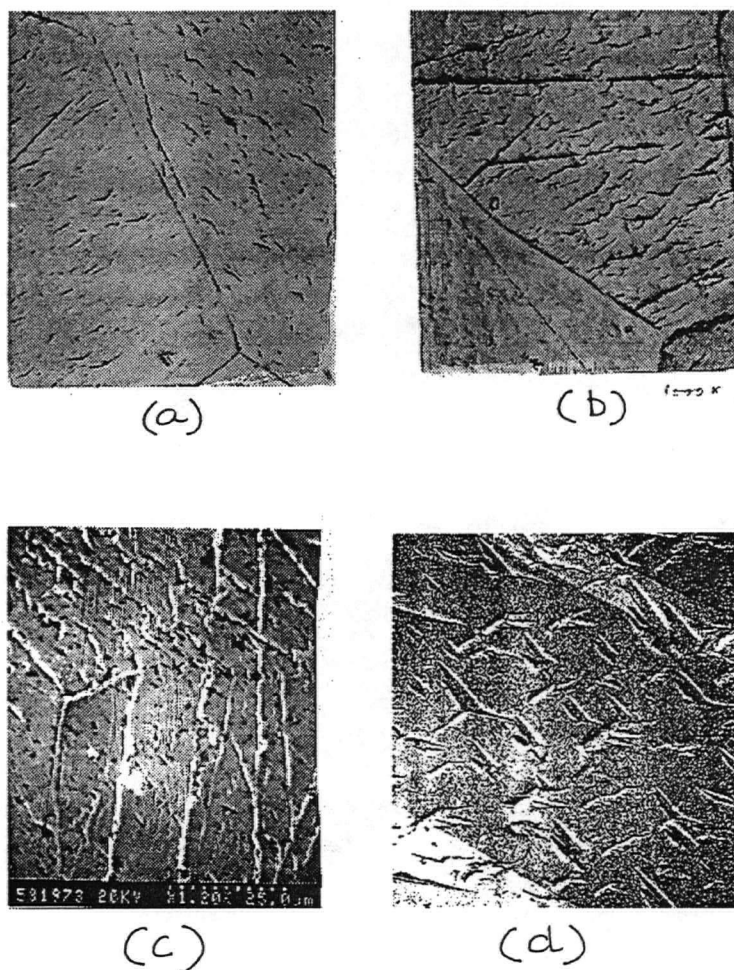


Figure [51] - Microphotos of 58 at. % Ni showing erosion after (a) 10 hours, (b) 14 hours and (c) 19.3 hours. Micrograph (d) is taken from ref. [35] (1000X)

of cavitation. Fig. [51](b) shows the coalescence of microcracks to generate larger cracks after 14 hours of cavitation exposure. The cracks are observed to arrest at grain boundaries. Fig. [51](c) shows the SEM photo after 19.3 hours of cavitation testing. Some cracks have crossed grain boundaries where there is total coherence of adjacent grains. Material loss is observed to occur at grain boundaries and in the direction of the cracks. Fig. 51(d) is taken from an earlier study on NiAl transformed by quenching [35]. The similarity of the fracture can be observed in Fig. 51(b) and 51(d).

62.2 at. % Ni:

The microstructure observed showed equiaxed grains with an average grain size of 128 μm . There was no cracking along grain boundaries during Rockwell "C" testing. Some microporosity was observed at grain triple point junctions with micro cracks originating from these porosities.

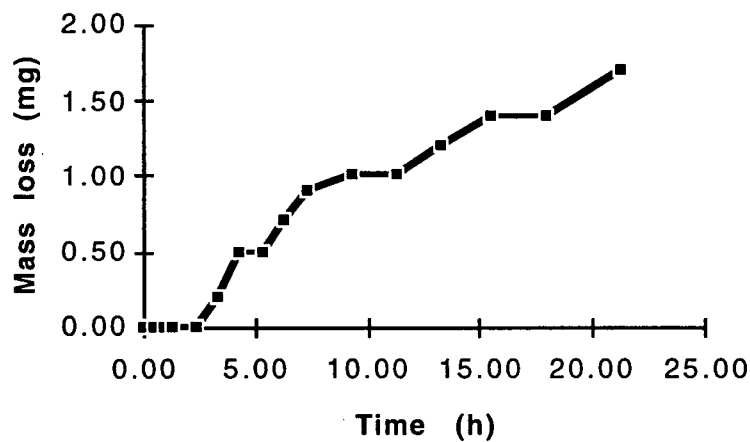


Figure [52] - Cavitation mass loss for 62.2 at. % Ni with $\pm 16 \mu\text{m}$ test amplitude and 600 grit finish

Fig. [52] shows the cavitation erosion mass loss test results for 62.2 at. % Ni

alloy with sample surface finish of 600 grit and test amplitude of $\pm 16 \mu\text{m}$. An incubation period of 3 hours was observed. The average mass loss rate was 1.15 mg/h. As cast microstructure (prior to cavitation testing) of the 62.2 at. % Ni composition showed thermal martensite occurring as shown in Fig. [53].

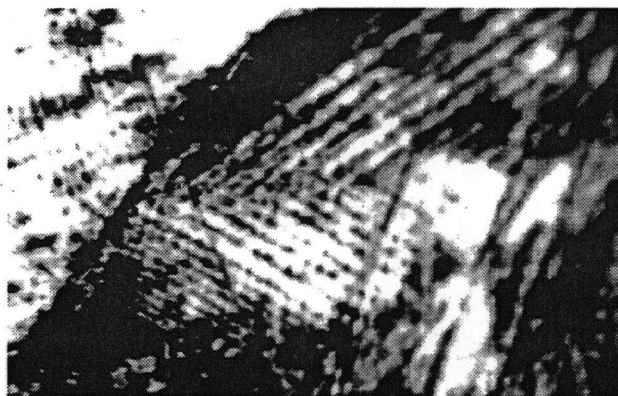


Figure [53] - Microphoto showing presence of thermal martensite in 62.2 at. % Ni as cast sample in uncavitated condition (500X)

Fig. [54] shows the cavitation test for amplitude: $\pm 25 \mu\text{m}$ /600 grit surface finish. An initial incubation period of 2 hours was observed. The average

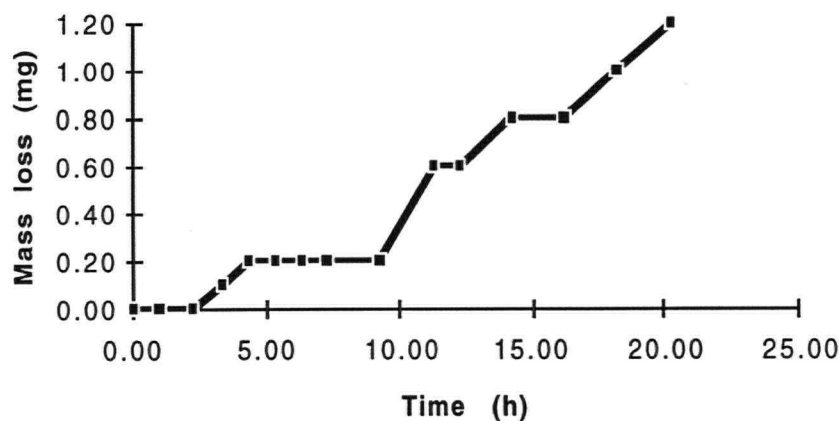


Figure [54] - Cavitation mass loss for 62.2 at. % Ni with $\pm 25 \mu\text{m}$ and 600 grit surface finish

mass loss rate was 0.07 mg./h. SIM was found after 5 hours of test duration. As before certain grains showed no cavitation when compared to others. Major cavitation was observed to occur in the grit marks rather than at the grain boundaries as seen in Fig. [55]. This could be due to the large compressive forces occurring at grain boundaries due to the martensite transformation occurring in the adjacent grains.

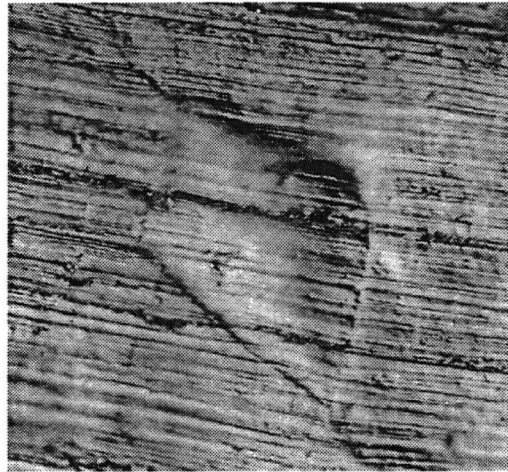


Figure [55] - Occurrence of major erosion in grit marks as compared to grain boundaries (1000X)

The cavitation test results with amplitude: $\pm 25 \mu\text{m}$ /surface finish: $0.05 \mu\text{m}$ are shown in Fig. [56]. There is a considerable increase in incubation time from the the two hours observed with the 600 grit finish to an incubation time of 9 hours. The average mass loss rate was 0.065 mg/h. It may be noted that even though the amplitude is higher, the erosion rate is lower than that observed with the lower amplitude of $\pm 16 \mu\text{m}$ and a similar surface finish of 600 grit.

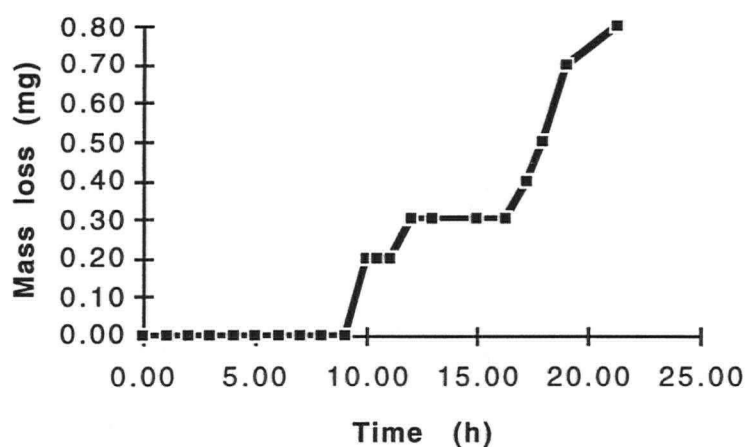


Figure [56] - Cavitation mass loss for 62.2 at. % Ni with $\pm 25 \mu\text{m}$ test amplitude and $0.05 \mu\text{m}$ surface finish

Fig. [57] shows martensite at 10 hours of cavitation testing time in one region of the sample. Fig. [58] shows a SEM photo of a triple point region where the three sets of thermal martensite have deformed sufficiently so that mass loss has occurred at the triple point as well as in a portion of a grain containing thermal martensite.

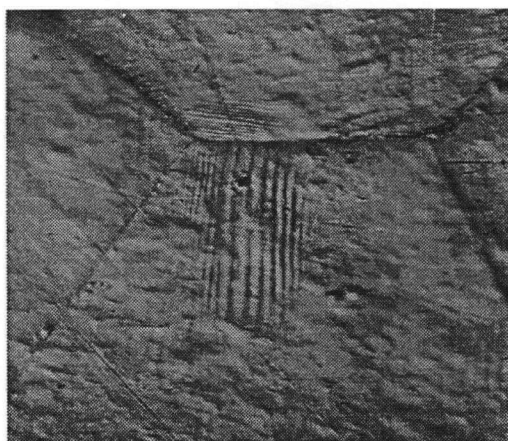


Figure [57] - Strain induced martensite after 10 hours of cavitation testing in 62.2 at. % Ni sample (1000X)

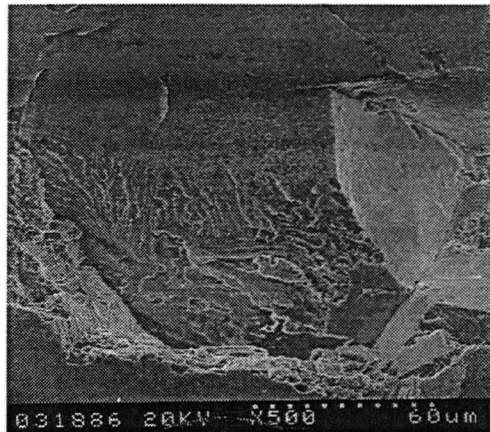


Figure [58] - SEM photograph of a grain in 62.2 at. % Ni after 10 hours of cavitation testing

Fig. [59] shows that after 12 hours the stress induced martensite transformation is occurring homogeneously throughout the grain. The width of the SIM plates seems to be finer than that of the thermal martensite plate.

The deformation of the martensite due to detwinning could give rise to the occurrence of cracks along the twin-twin boundary and also along the martensite plate-twin boundaries. Coalescence of these cracks will lead to mass loss occurrence ultimately.



Figure [59] - Optical microphotograph showing homogeneously formed strain induced martensite in 62.2 at. % Ni sample during cavitation testing (500X)

The XRD graphs at different time periods of the test are shown in Fig.[60] for the 62.2 at. % Ni sample.

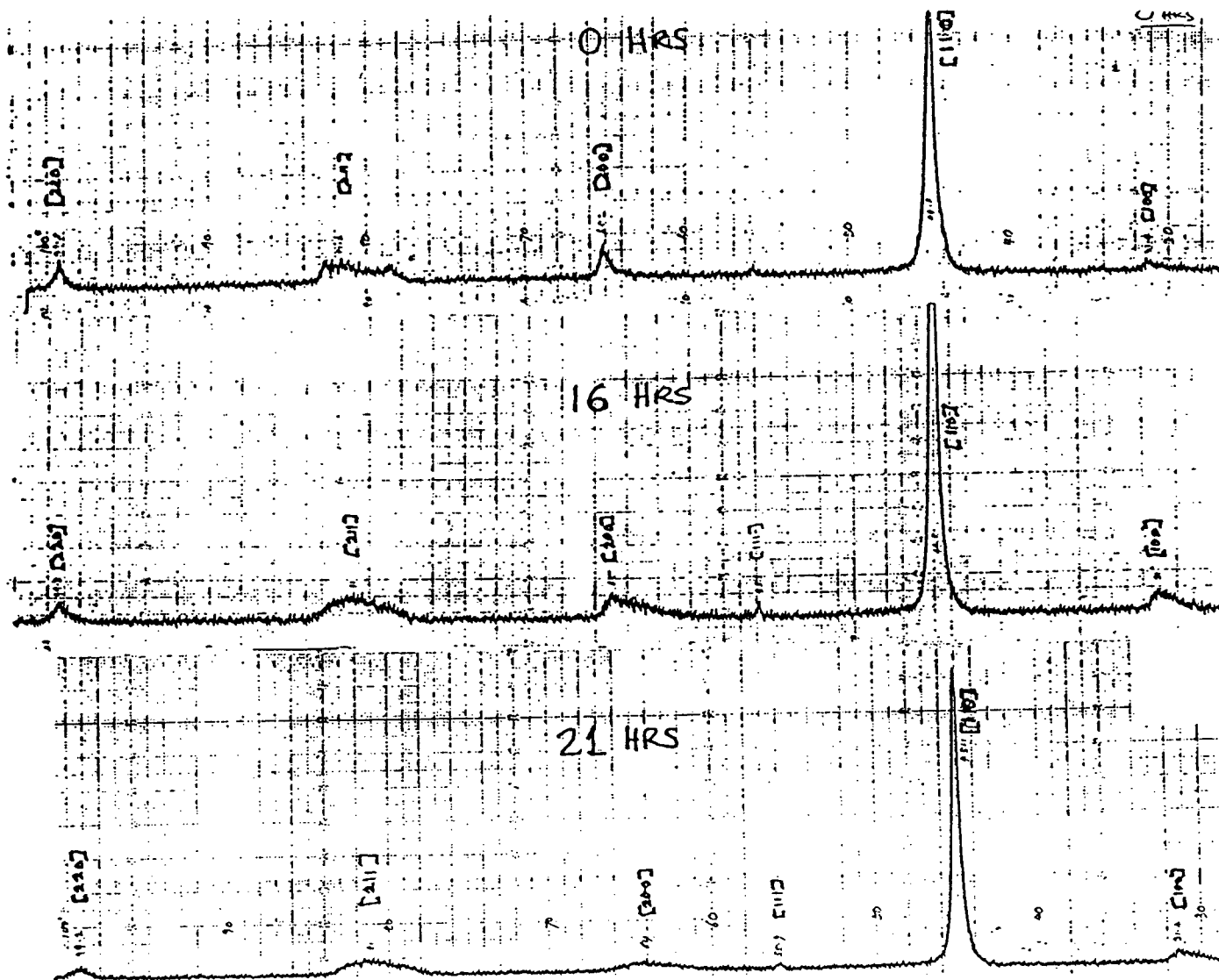


Figure [60] - XRD graphs at different time periods for 62.2 at. % Ni during cavitation erosion

5.0 DISCUSSIONS

The influence of various parameters on the cavitation erosion behaviour of nickel aluminides are discussed here . Cavitation erosion rates of the nickel aluminides are compared with these and other well known materials.

MICROCRACKS

Ni₃Al:

The Ni₃Al sample with an existing crack showed an average mass loss rate of 4.8 mg./h. whereas an uncracked Ni₃Al sample showed a mass loss rate of 0.4 mg./h. The difference in the rate of mass loss between these two samples indicates that the energy input of the imploding bubble is dissipated differently in these samples. In the case of a crack being present in Ni₃Al, the energy is utilized in propagating the existing crack and for initiating new cracks. However Ni₃Al in the absence of defects would utilize this energy for plastic deformation. The implication of the observation made here is that if Ni₃Al is to be used as an overlay for cavitation erosion, the overlay must remain free of cracks. The cracked overlay would be eroded roughly 10 times faster than would a crack free layer.

It is known that ductility can be imparted to Ni₃Al through addition of small amounts of boron which segregates at the grain boundaries [14]. An Ni₃Al alloy containing a small amount of boron and zirconium has been tested earlier by Richman et al [9] for its cavitation resistance. The test method used was similar to that of the present work. However, the amplitude for testing

was $\pm 16 \mu\text{m}$ in the present work compared with $\pm 25 \mu\text{m}$ in Richman et. al. work. The erosion rate obtained by Richman et. al for the boron/zirconium containing Ni_3Al was 5.8 mg/h. The present work with unalloyed Ni_3Al tested at $\pm 16 \mu\text{m}$ amplitude gave values of 4.8 mg/h. for the cracked sample and 0.4 mg/h. for the uncracked one. Although a direct comparison of the data obtained in the present work with that of Richman et. al is not meaningful due to the difference in the test amplitude, it appears that avoiding cracking through the addition of boron results in a trade-off in the cavitation resistance of the material.

NiAl:

In the case of NiAl, microcracks originating at microporosity do not seem to lower the cavitation erosion resistance, specially in the 58 and 62.2 at. % Ni. compositions. It could be because the energy is absorbed in transformation to martensite in these compositions. The microcrack propagation is possibly arrested due to the deformation by the process of crack blunting or crack shielding [65]. For 47 to 53 at. % Ni compositions, the grain boundaries are weaker leading to fracture occurring intergranularly rather than through the propagation of microcracks present at the outset of the cavitation erosion process.

COMPOSITION

Ni₃Al:

As only a single composition of 75 at. % Ni was tested for the Ni₃Al phase, it is not possible to comment on this aspect in Ni₃Al for cavitation erosion resistance.

NiAl:

Fig. [61] shows the variation of the mass loss rate with the composition of this

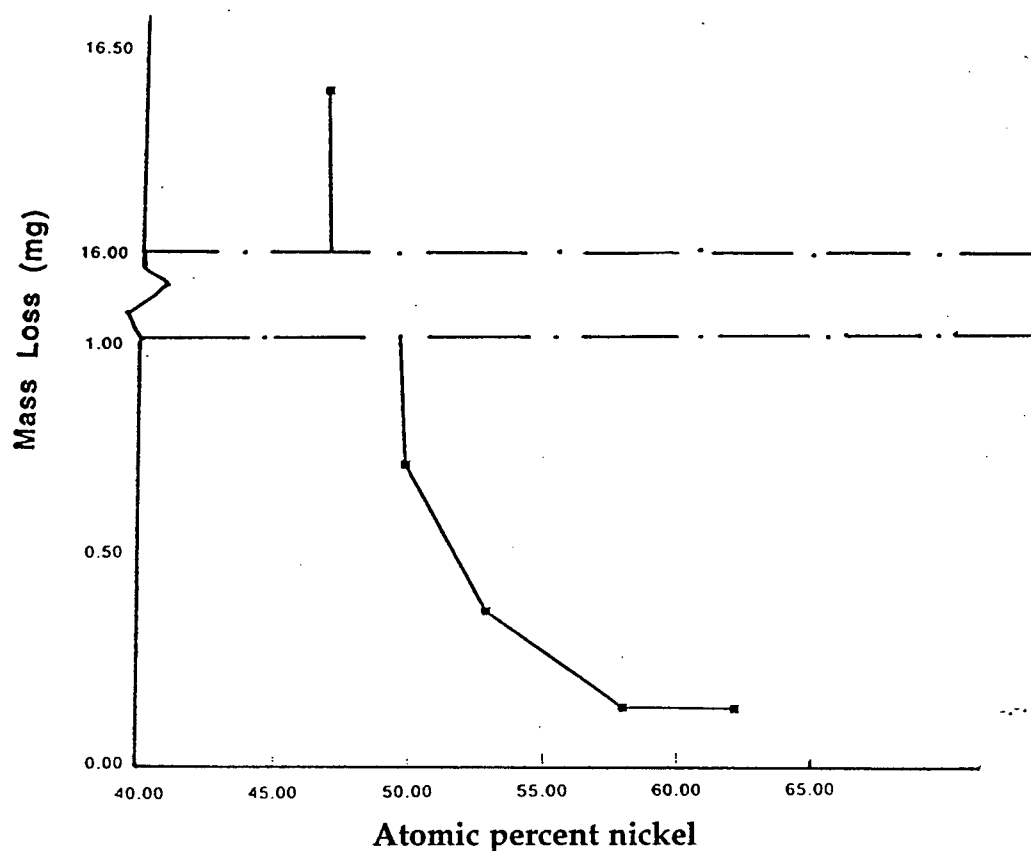


Figure [61] - Variation of mass loss rate due to cavitation erosion in NiAl with atomic percent nickel

phase in the range of 47 - 62.2 at. % Ni. It is seen that as the atomic percent Ni increases there is a decrease in the mass loss. It has been observed by Ball [34]

that 57 at. % Ni shows strain induced martensite transformation when a single crystal of this alloy is compressed along the [001] axis. Metallographic studies in the present investigation confirmed the occurrence of martensitic transformation products, in the as cast or cavitated samples, having composition of 58 and 62.2 at. % Ni. The presence of plateaus of no mass loss has been observed in the present work with compositions that clearly exhibit stress induced martensitic transformation (58 and 62.2 at. % Ni). A small plateau is also observed with 53 at % Ni as seen in Fig. [40], which may suggest that the stress induced martensitic transformation possibly occurs at the high strain rate imposed by cavitation erosion. However, the transformation product was not observed optically in 53 at. % Ni sample due to the rough surface finish (600 grit) of the sample.

Cast microstructures of 58 and 62.2 at % Ni had thermal martensite colonies. These heterogeneous regions were mostly present at grain triple point junctions. The percentage of thermal martensite increased with atomic per cent nickel. It has been reported by Kim and Wayman [43] that the M_s temperature increases with nickel content. Kim and Wayman's data are replotted in Fig. [62] by the present author.

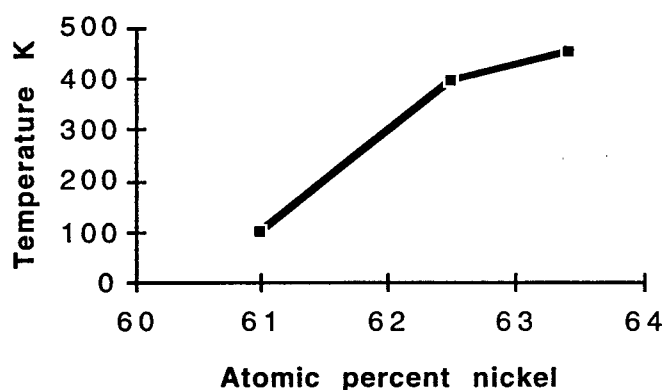


Figure [62] - M_s temperature variation with atomic percent nickel in NiAl

As noted earlier in Fig. [53] thermal martensite was present in the 62.2 at. % Ni - NiAl. The thermal martensite is of the $L1_0(3R)$ type and is internally twinned as shown by Enami et al [42].

The martensite is thermoelastic as shown by Waymann and Au [47]. The deformation, of the martensite which is internally twinned, occurs by a detwinning mechanism. In the present investigation, the 58 at.% Ni composition shows the highest cavitation erosion resistance (0.05 mg/h. for 0.05 μm finish and $\pm 25 \mu\text{m}$ amplitude in Table [IX]. This composition also shows a SIM transformation in regions of the grain where no thermal martensite is present. The energy of the bubble implosion is primarily absorbed in deformation of the thermal martensite and secondarily towards transformation. As SME is occurring it could lead to increased strain at twin-twin and twin-grain boundaries. Subsequent mass loss begins with fracture initiation as shown in Fig. [51] which could be due to the deformation of both the thermal martensite and the SIM. Crack propagation and coalescence seem to prevent any further SME being observed.

MECHANICAL PROPERTIES

Richman and McNaughton [65] have tried to correlate the cavitation erosion behaviour with mechanical properties of cobalt alloys and stainless steels. Their studies indicate that stacking fault energy (SFE) correlates closely with the cavitation erosion resistance of most alloys. Thus alloys with lower SFE, according to Richman & McNaughton, are capable of phase transformations and hence exhibit better cavitation erosion resistance.

Ni₃Al:

The mechanical properties of Ni₃Al along with the rate of cavitation erosion for stoichiometric Ni₃Al are shown in Table [V].

Composition, at. % Ni	Condition	Yield* Strength, psi	Tensile* Strength, psi	Extensometer* Elongation, %	Cavitation Erosion, mg./h.
75	As-cast	12,000 13,000	30,600 26,700	1.1 .9	0.4

* Data from reference [17]

Note: 1 psi \equiv 6.894 kPa

As tests were not carried out for deviations from stoichiometry in Ni₃Al, a discussion on this aspect is not possible.

NiAl:

The mechanical properties of hardness, tensile strength, etc. for the range 47 - 62.2 atomic percent nickel are already shown in Table [III]. The rates of cavitation erosion for the intermetallic compound with a 47 - 62.2 at. % Ni range are shown in Table [VI].

Table VI - Cavitation Erosion Rate of NiAl in the composition range of 47 - 62.2 atomic percent nickel with 600 grit and $\pm 16 \mu\text{m}$ test amplitude	
Atomic percent Nickel	Average Mass Loss Rate (mg./h.)
47	16.4
50	0.7
53	0.35
58	0.12
62.2	0.115

Although there is an increase of hardness on both sides of the stoichiometric composition of NiAl, the cavitation erosion rate does not show a relationship to the hardness change. Most alloys of similar groups show a good correlation between cavitation erosion and hardness as is seen in Table [VII]. This does not hold for the intermetallic compound NiAl.

Fig. [63] shows the variation of erosion rate with the tensile strength in NiAl in the atomic range 50 at. % Ni to 62.2 at. % Ni. It is observed that as the tensile strength increases, the erosion rate decreases.

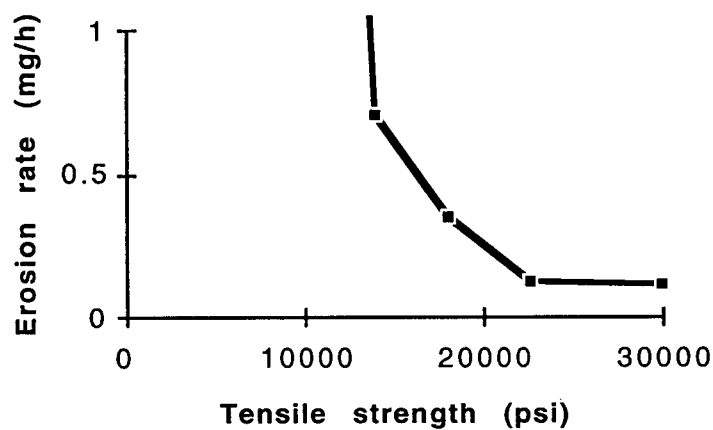


Figure [63] - Variation of tensile strength and cavitation erosion rate with atomic percent nickel

Note: 1 psi = 6.894 kPa

Table VII - Cavitation Damage Resistance of Various Materials (From reference [59])									
Material (arranged in order of increasing hardness)	Compo- -sition percent	Hardness (Brinell)	Ulti- -mate tensile strengt h (psi x 10 ³)	Modulus of elasti- -city (psi x 10 ⁶)	Depth of Cavitation Damage Hole in microns (10 ⁻⁴)				
					10 sec	1 min	15 sec	30 min	1 h.
Aluminum		16	16	10	10	80			
Titanium (Annealed)		58	79	16	43	78			
Nickel		90	50	30	80	115			
Molybde- -num		120	57	50		10	25	60	100
Brass	Cu 70, Zn 30	123	56	13	135	128			
Stainless Steel	Cr 18, Ni 8	163	102	29	15	28			
Titanium 75-A		203	80	16	30	66			
Steel (4130)		258	130	30	32	55			
Tungsten		350	597	51	0	0	3		
Titanium 130-A	Ti 92, Mn 7.9	351	130	16	0	3	16		
Colmonoy		400	61		0	3	18	34	

The area under the stress strain curve is perceived to be a correlating factor [60] with cavitation erosion resistance in most alloys. Since stress strain curves are not available for NiAl, the validity of such a correlation cannot

be verified in the case of NiAl.

PHASE TRANSFORMATION

Observations of superior cavitation resistance due to twinning have been made by Vaidya, Mahajan and Preece [55] in the study of cobalt single crystals. However, Woodford [60] found no correlation between transformation and erosion when testing Stellite 613 alloy. Also Richman and Rao [9] have found that for NiTi ordered intermetallic alloy the parent B2 austenitic phase was superior to the thermal martensitic phase when each was tested for cavitation erosion.

In Ni₃Al no phase transformation was observed. Hence the effect of phase transformation on cavitation erosion cannot be discussed for the stoichiometric Ni₃Al.

In NiAl, the present investigation confirms the strain induced phase transformations observed by several investigators [30, 42, 48]. Thermal martensite was also found, which resulted from the cooling from liquid phase during casting of 58 and 62 at. % Ni compositions.

The 62 at. % Ni alloy shows thermally induced martensite present in certain areas. The alloy also shows a SIM transformation which could be responsible for the excellent cavitation erosion resistance of this composition as seen in Fig. [56]. However, in a cavitation study with B2 structure, stoichiometric NiTi did not show better cavitation erosion resistance for the

thermally induced martensite sample as compared to the austenite B2 phase sample. The thermally induced martensite would undergo deformation by detwinning, leading to initiation of fracture at twin-twin boundaries or twin-plate boundaries and subsequent material loss. The observations of this investigation confirm a similar process in NiAl. It is proposed that avoidance of thermal martensite could further improve the cavitation erosion resistance of NiAl.

Strain induced martensite with internally twinned structure is reported to show SME [43] in NiAl. A larger percentage of SIM as compared to thermal martensite might exhibit a better cavitation erosion due to an increased SE effect, because of faster strain recovery. Also the SIM plates are narrower than the thermal martensite as seen from Fig. [58](b) and Fig. [59]. This would reduce the free mean path for dislocation motion leading to faster work hardening [67] rates and an increased cavitation erosion resistance. Future investigations may verify this by testing as cast 58 at. % Ni and 62.2 at. % Ni compositions of NiAl without the presence of thermal martensite. This would confirm any correlation between transformation and erosion in NiAl.

The 62.2 at. % Ni showed a larger percentage of thermally induced martensite (TIM) than did 58 at. % Ni. Both these compositions show a SIM transformation. On being subjected to cavitation erosion, the 58% at. Ni sample showed a higher SIM transformation as it has a lesser TIM percentage. As the strain accumulates in the areas where TIM has not formed, these areas

of the grain transform to SIM in a homogeneous manner similar to chemical spinoidal decomposition [66]. As proposed earlier, a larger % of SIM will lead to a SE effect which is observed in case of 58 at. % Ni leading to a better cavitation erosion resistance than 62.2 at. % Ni.

GRAIN ORIENTATION

During TEM analysis of cavitated samples of Ni_3Al , March [61] has found dislocation substructures caused by the cavitation process. Thus strain energy would be dissipated in the formation of the substructure thereby delaying the onset of stress accumulation at the grain boundaries, where mass loss occurs. Also, the presence of inclusions may assist the process of substructure development. This could be the reason why no cavitation erosion was observed in certain areas of the stoichiometric Ni_3Al , as seen in Fig. [31].

NiAl: Fig. [51] and Fig [59] show that in both the 58 at. % Ni and 62.2 at. % Ni. there are some grains which have not undergone erosion, even after prolonged exposure. These grains probably had undergone SIM transformation. However some grains eroded earlier than did others although all had undergone SIM transformation. Such preferential erosion indicates a strong grain orientation effect on cavitation erosion.

The anisotropic behaviour of the mechanical and physical properties of NiAl has been studied earlier [28]. The SIM transformation remains strongly

dependent on crystal orientation [34]. Hence depending on grain orientation and the anisotropic properties, the shear strain component will differ leading to variations in the percentage of SIM regions in different grains. A large percentage of SIM will be observed in the [001] "hard" direction because of faster strain accumulation. Plastic deformation due to crystallographic slip does not occur readily in this "hard" orientation. However, grains oriented in the [001] direction should show better cavitation erosion because of the ease of SE in this orientation [48]. The strain associated with super elasticity has the highest value for the [001] oriented crystals and occurs at the lowest stress level when compared with [110] and [111] orientations in 64 at. % Ni alloy single crystals deformed at a low strain rate at room temperature. It has been found that if the stress is applied along the [001] direction, elongations as high as 13% are observed as seen from Fig. [42]. A single twinned martensite orientation [57] was associated with the 13% elongation.

Residual Stresses

Residual stresses caused due to the casting, fabrication or welding overlays of Ni₃Al or NiAl may play a role in the applications of these materials.

Ni₃Al: The stoichiometric Ni₃Al samples were given a homogenization anneal. However, further stresses could have been reintroduced due to the cutting and grinding operations. The effects of such stresses on subsequent erosion resistance were not investigated.

As this aspect has not been investigated for Ni₃Al it cannot be discussed in this study.

NiAl: It was observed in the present study that residual stresses caused by casting and subsequent specimen preparation procedure such as grinding resulted in cracking and an associated mass loss of samples with nickel atomic percent between 47 and 53. This observations suggests that compositions in this range are prone to mass loss during cavitation erosion as a consequence of residual stresses.

Samples containing 58 and 62.2 at. % Ni did not show early signs of cracking. Thermally induced martensitic transformations, which were observed, possibly relieved the thermal stresses.

During grinding and polishing, these higher nickel containing specimens do not undergo cracking due to their ability to absorb strain through SIM transformations. This feature of 58 and 62.2 at % Ni containing alloys makes them desirable for practical applications, which invariably involve grinding for obtaining the desired contour. However, the residual stress may yet affect the erosion rate in a manner similar to AISI 304L material which also undergoes SIM transformations. This aspect of the cavitation erosion needs further examination.

COMPOSITION, SURFACE FINISH AND CAVITATION INTENSITY

Fig. [64] shows the variation of the incubation period with the nickel content of the intermetallic compound NiAl. The data are also shown in Table [VIII].

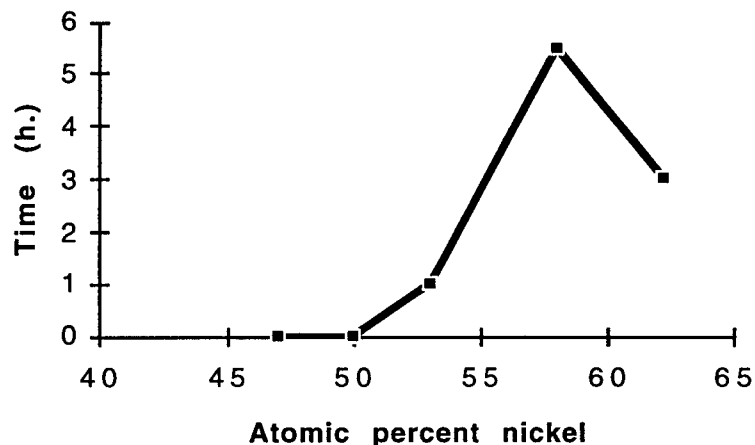


Figure [64] - Variation of incubation period with nickel content in NiAl for 600 grit surface finish and $\pm 16 \mu\text{m}$ test

Table VIII - Incubation Period (h.)			
at. % Ni	Amplitude $\pm 16 \mu\text{m}$ 600 grit finish	Amplitude $\pm 25 \mu\text{m}$ 600 grit finish	
		600 grit finish	0.05 μm finish
47	0
50	0
53	1
58	5.5	1.5	6
62.2	3	2	9

In Fig. [64] an incubation period was not observed for the 47 and 50 at. % Ni compositions. Between 50 and 58 at. % Ni a monotonic increase is observed. However, the 62.2 at. % Ni composition showed a lower incubation period than the 58 at. % Ni. At higher intensities of cavitation (amplitude $\pm 25 \mu\text{m}$), on the other hand, 62.2 at. % Ni gave a higher incubation period than did 58

at. % Ni both under ($0.05\mu\text{m}$) surface finish. The actual values of incubation period were significantly higher for the finer finished samples.

Fig. [65] shows the variation of the average erosion rate with atomic percent

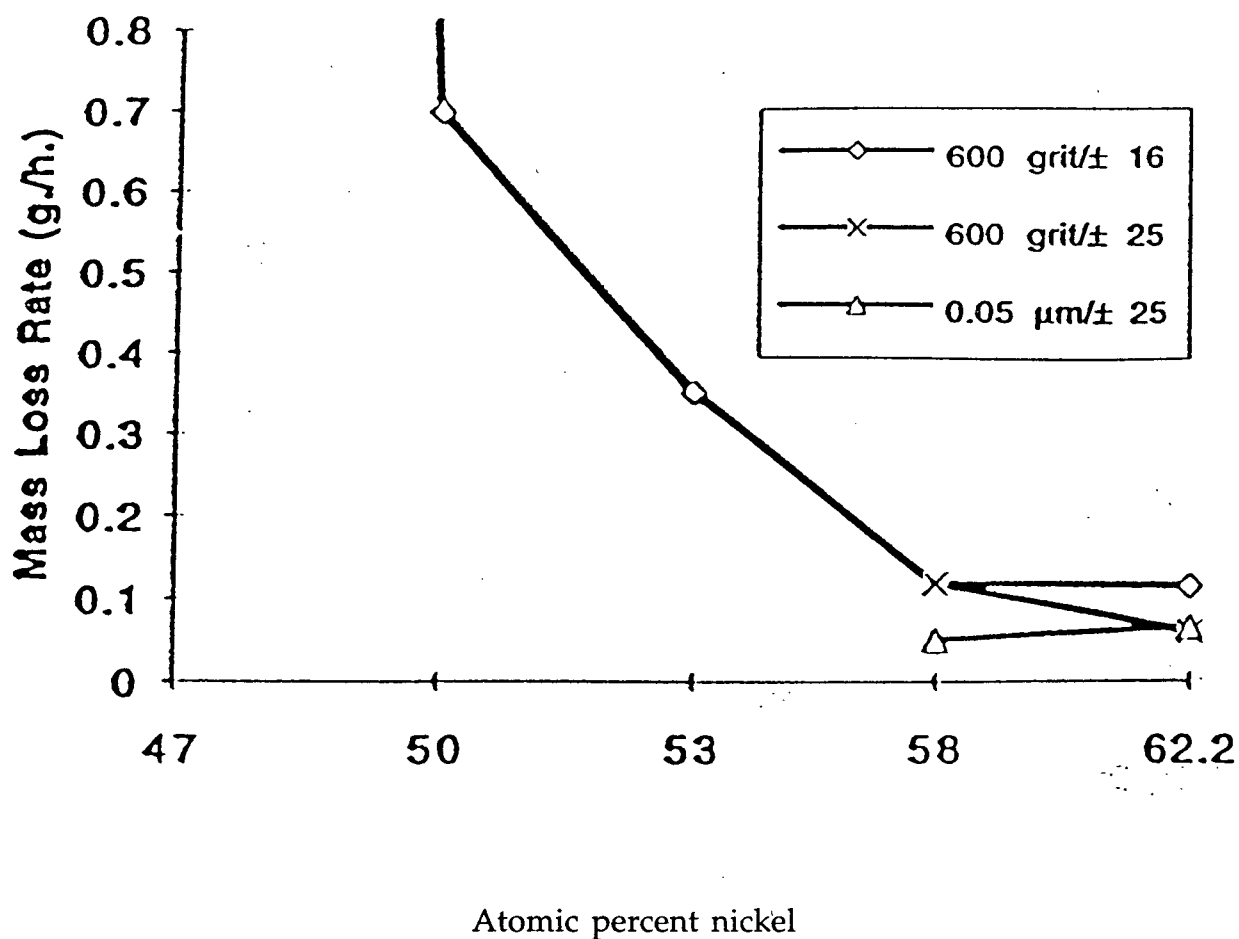


Figure [65] - Effect of cavitation intensity and surface finish on mass loss rate for 47 - 62.2 at. % Ni in NiAl

nickel for the intermetallic compound NiAl, at the two cavitation intensities (amplitudes of oscillation $\pm 16\text{mm}$ and $\pm 25\mu\text{m}$) and for the two types of surface finish. The data are also shown in Table [IX].

Table IX - Erosion Rates			
at. % Ni	Average Mass Loss rate (mg./h.)	Surface Finish	Amplitude (μm)
47	16.4	600 grit	$\pm 16 \mu\text{m}$
50	0.7	600 grit	$\pm 16 \mu\text{m}$
53	0.35	600 grit	$\pm 16 \mu\text{m}$
58	0.12	600 grit	$\pm 16 \mu\text{m}$
	0.12	600 grit	$\pm 25 \mu\text{m}$
	0.05	0.05 μm	$\pm 25 \mu\text{m}$
62.2	0.115	600 grit	$\pm 16 \mu\text{m}$
	0.06	600 grit	$\pm 25 \mu\text{m}$
	0.065	0.05 μm	$\pm 25 \mu\text{m}$

At the low intensity ($\pm 16\mu\text{m}$) a monotonic decrease in the average cavitation erosion rate occurs between 47 at. % Ni and 62.2 at. % Ni. At the higher cavitation intensity ($\pm 25\mu\text{m}$), the erosion rate of 58 at. % Ni sample remained unchanged from that at the lower intensity when the surface finish was rough (600 grit). The erosion rate decreased with the finer surface finish in the case of 58 at. % Ni sample, as is normally observed with other materials. In the case of 62.2 at. % Ni alloy samples, on the other hand, surface finish did not affect the erosion rate at the higher intensity of cavitation. The actual value of the erosion rate of the 62.2 at. % Ni alloy at the higher cavitation

intensity, however, was lower than that observed at the lower intensity. The latter observation is in contrast to the behaviour normally observed in other materials. Normally the erosion rate increases with cavitation intensity as seen in Fig. [66].

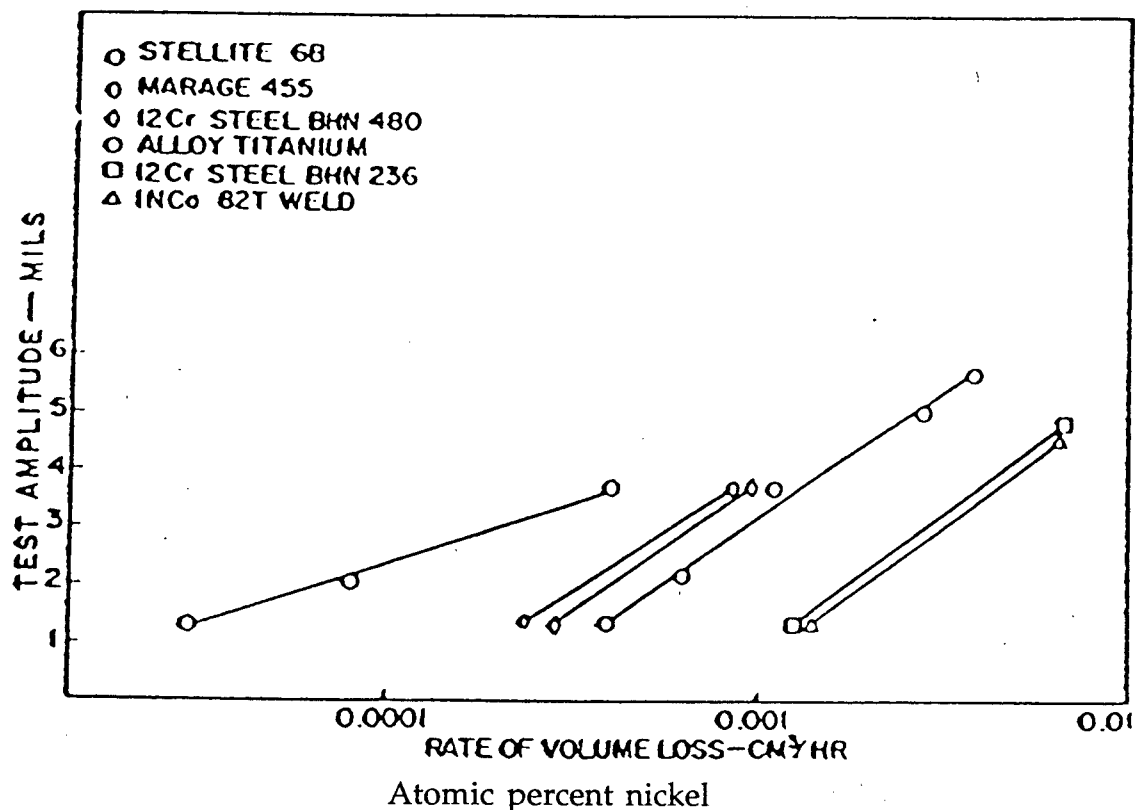


Figure [66] - Variation of erosion rate with cavitation intensity for alloys - Ref.[67]

The reason for the anomalous behaviour of the 62.2 at. % Ni composition is not clear. However, this observation is of considerable practical importance for two reasons. First the protective material need not be given a fine finish and secondly, the erosion resistance would be better the higher the cavitation intensity.

COMPARISON OF NiAl WITH OTHER CAVITATION RESISTANT
MATERIALS

As compared with Ni₃Al, which has an erosion rate at the lower intensity ($\pm 16\mu\text{m}$) of 0.4 mg./h., the two NiAl compositions of 58 and 62.2 at. % Ni have erosion rates which are about a third (0.12 mg./h.) at the same intensity. March has conducted studies on Ni₃Al doped with boron (0.02% wt.) for the IC-50 alloy (Zr = 0.6% wt.) and finds that the cavitation erosion rate is 5.8 mg./h. when tested in a similar manner [9].

Fig. [67] shows the cavitation erosion rate for various alloys of industrial

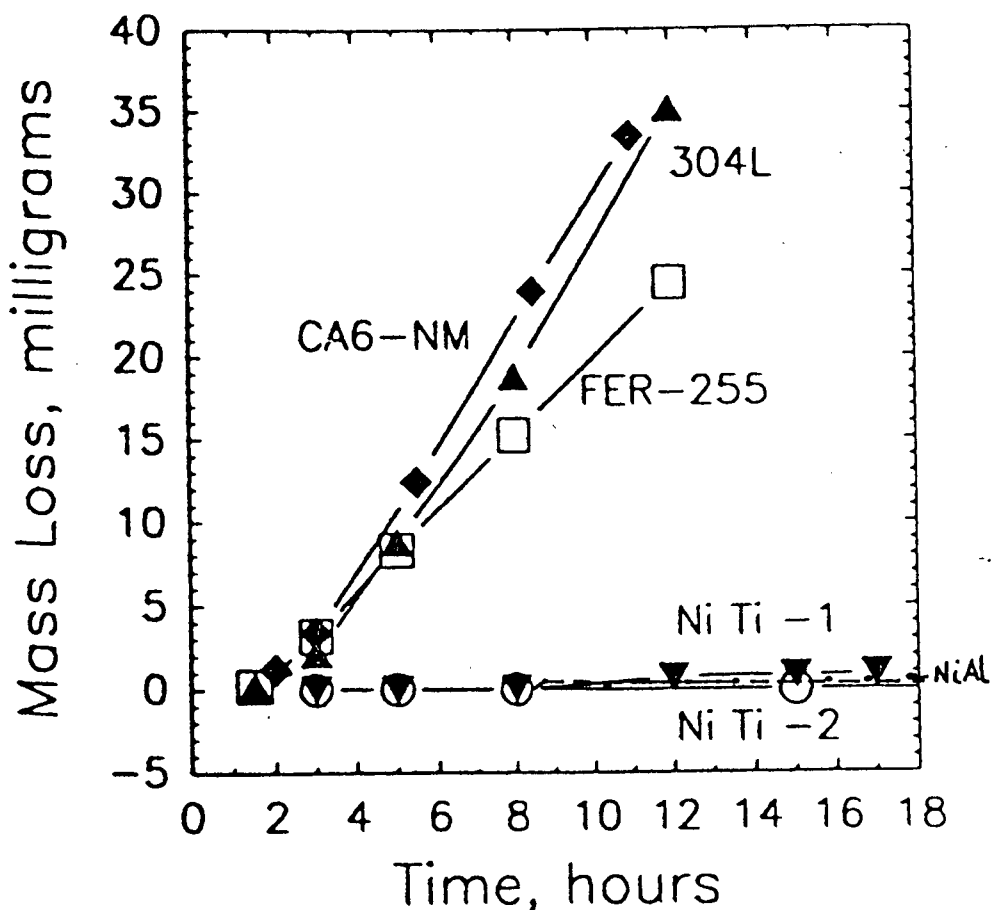


Figure [67] - Comparison of cavitation erosion rates for tested industrial alloys tested for cavitation erosion by the stationary specimen method - Ref. [9]

significance when tested for cavitation erosion using a test method similar to of the present work. It can be seen that NiAl compositions, both 58 at. % Ni, and 62.2 at. % Ni show comparable cavitation resistance to stoichiometric NiTi as found by Richman and Rao. The incubation period for NiTi appears to be longer than that of 58 - 62.2 at. % Ni - NiAl. However, processing of NiTi is expensive and requires high vacuum (10^{-6} torr.). Further the Ni-Ti phase diagram indicates NiTi is a stable phase only above 630°C . To retain the cavitation resistant high temperature austenite (β NiTi) the material must be quenched with precise compositional control.

NiAl on the other hand is easy to manufacture by conventional processing. It is also relatively cheaper than NiTi or Stellite alloys. Further, there is a large compositional field over which NiAl is stable at 400°C and possibly below this temperature. All of this combined with the excellent cavitation erosion resistance for the 58 at. % Ni - 62.2 at. % Ni, make NiAl a suitable material where cavitation erosion resistance is required.

6.0 CONCLUSIONS

In general the cavitation erosion of nickel aluminides is comparable to well known cavitation resistant materials such as cobalt based alloys and NiTi. The following specific conclusions have been arrived at from the present study:

1. The cavitation erosion rate of the intermetallic compound NiAl decreases with increasing nickel content in the composition range of 47 - 62 at % Ni.
2. The martensitic transformation plays a role in determining the cavitation resistance of NiAl intermetallic compound. Thermally induced martensite reduces the cavitation resistance whereas stress induced martensitic transformation enhances the cavitation erosion resistance.
3. Normally, as the cavitation intensity (amplitude of oscillations) increases, the mass loss rate increases i.e. the cavitation erosion resistance is reduced. The present study indicates that this trend holds in case of 58 at. % Ni. However, in the case of 62.2 at. % Ni an increase in cavitation erosion resistance was observed at a higher cavitation intensity. The reason for this latter anomalous behaviour is unclear.
4. The intermetallic compound NiAl containing about 60 atomic % Ni has commercial potential as a cavitation resistant material for applications in hydraulic machinery.

5. Ni_3Al has good cavitation erosion resistance. However, the erosion rate increases dramatically in the presence of prior cracks on the surface. Addition of boron may eliminate cracking. However, its influence on the cavitation erosion resistance may not be beneficial.

7.0 FUTURE DIRECTION

Although the present study has provided insight into the cavitation erosion behaviour of Ni_3Al and NiAl , further investigations would be desirable.

Two major items have been identified:

1. Stress and orientation dependence of the stress induced martensitic transformation may be further investigated using single crystals of various orientations and at compositions of 58 - 62.2 at. % Ni in particular.
2. The lower cavitation erosion rate at a higher cavitation intensity in 62.2 at. % Ni compositions may be investigated further to take advantage of this material for practical applications.
3. The effect of boron addition on the cavitation erosion resistance of Ni_3Al may be investigated further

REFERENCES

1. "Canadian Energy - Supply and Demand 1993-2010", Technical Report, National Energy Board, Ottawa, December 1994, pp. 536-537.
2. Carolyn M. Hansson and Inge L.H. Hansson, "Cavitation Erosion", ASM-Metals Handbook, Vol (18)1992, pp. 214-220.
3. T. Okada, Y. Iwai, S. Tanaka & P. Awazu, "A Study of Cavitation Bubble Vapour Collapse Pressures and Erosion", Parts I and II, Wear 133, 1989, pp. 225-243.
4. A. Ball, "The Erosion of Ceramic Materials: A Comparative Study", Proceedings of the 34th Annual Conference of Metallurgists, August 1995, Vancouver, Canada, pp. 19-24.
5. C.T.L. Webster and F. Havelock, "Alternative Coatings for the Protection of Hydraulic Turbines from Cavitation Erosion", Canadian Electrical Association Final Report on Contract G274, September 1987, pp. 6-12.
6. A. Akhtar, A.S. Rao and D. Kung, "Cavitation Erosion of Stainless Steel, Nickel and Cobalt Alloy Weld Overlay Materials", Proceedings of the ASM Conference on Coatings and Bimetals for Aggressive Environment, Ed. Richard D. Sisson, Jr., 1984, pp. 124-142.
7. A. Karim, "Cavitation Erosion of a Duplex Stainless Steel", Materials Science and Engineering, 1987, pp. 191-203.
8. I. Baker & P.R. Munroe, "Properties of B₂ Compounds", High Temperature Aluminides and Intermetallics - The Minerals, Metals and Materials Society, 1990, pp. 160 - 168.
9. R.H. Richman, A.S. Rao and D.E. Hodgson, "Cavitation Erosion of Two NiTi Alloys", Wear 157, 1992, pp. 401-407.
10. M. J. Marcinkowski, "Ordered Structures", Metals Handbook Vol.(9) - Microstructures, 1985, pp. 681-683.
11. V. K. Sikka, "Nickel Aluminides - New Advanced Alloys", Materials and Manufacturing Processes 4(1), 1989, pp. 1-24.

REFERENCES (cont.)

12. C. T. Liu & V. K. Sikka, "Nickel Aluminides for Structural Use", Journal of Materials, May 1986, pp. 19-21.
13. Ram Darolia, "NiAl Alloys for High Temperature Structural Application", Journal of Materials, March 1991, pp. 44-49.
14. W. Yan, I.P. Jones, R.E. Smallman, "The Effect of Boron Dopant on Dislocation Configurations in Polycrystalline Ni₃Al", Scripta Metallurgica et Materialia, Vol. 21, 1987, pp. 1511-1515.
15. E.M. Schulson and D.R. Barker, "Effect of Grain Size on the Tensile Ductility of NiAl", Scripta Metallurgica, Vol. 17, 1983, pp. 519-521.
16. H. Hosoda, T. Shinoda, Y. Mishinara, T. Suzuki, "Vacancy Properties of Ordered Intermetallic Alloys in the NiAl System", Computer Aided Innovation of New Material II ed. M. Doyanna et al, 1993, pp. 1481-1482.
17. E. M. Grala, "Investigation of NiAl and Ni₃Al", Mechanical Properties of Intermetallic Compounds, Ed. J. H. Westbrook, John Wiley and Sons, Inc., 1959, pp. 71 -85
18. Baode Sun et al, "The Ductility of La-Doped Rapidly solidified NiAl", Scripta Metallurgica et Materilia, Vol. 33, No. 7, 1995, pp. 1145-1149.
19. A. Ball, "The Observations of a Martensitic Transformation in the Compound NiAl", Metal Science Journal, 1967, pp. 47-48.
20. C.C. Koch, "Rapid Solidification of Intermetallic Compounds", International Metals Review, Vol. 33, No. 4, 1988, pp. 201-219.
21. M. Sahoo, A. Lui, G. Morin, V.K. Sikka, "Mechanical Properties and Erosion Behaviour of Nickel Aluminides", Canadian Metallurgical Quarterly, Vol. 30, No.1, 1991, pp. 55-69.
22. C.T. Liu, C.L. White and J.A. Horton, Acta Metallurgica et Materilia, Vol. 33, 1985, pp. 213-215.

REFERENCES (cont.)

23. H. Kung, D.R. Rasmussen and S.L. Sass, "The Local Compositional; Order and Dislocation Structure of Grain Boundaries in Ni₃Al", Kulver Academic Publishers, Netherlands, Eds. C.T. Liu et al - Ordered Intermetallics-Physical Metallurgy and Mechanical Behaviour, 1992, pp. 315-370.
24. K.T. Ansf, "Grain Boundary Engineering", Canadian Metallurgical Quarterly, Vol. 33, No. 4, 1994, pp. 265-274.
25. N.S. Stoloff, "Physical and Mechanical Metallurgy of Ni₃Al and Its Alloys", International Metals Reviews, Vol. 34, No. 4, 1989, pp.153-183.
26. M. L. Weaver, "Investigation of Strain Aging in the Ordered Intermetallic Compound β -NiAl", NASA Contractor Report # 198364-Personal communications, July 1995.
27. K. Vedula and P.S. Khadikar, "High Temperature Aluminides and Intermetallics", The Minerals, Metals and Materials Society, Eds: S.H. Wang, C.T. Liu, D.P. Pope, J.O. Stiegler, Warrendale, P.A., 1990, pp. 197-198.
28. D.B. Miracle, "The Physical and Mechanical Properties of NiAl", Acta Metallurgica et Materilia, Vol. 41, No.3, 1993, pp. 649-684
29. S.V. Raj, R.D. Noebe and R. Bowman, "Observations of the Brittle to Ductile Transition Temperatures of B2 Nickel Aluminides with and without Zirconium", Scripta Metallurgica, Vol. 23, 1989, pp. 2049-2054.
30. A. Ball and R.E. Smallman, "Deformation Properties and Electron Microscopy Studies of the Intermetallic Compound NiAl", Acta Metallurgica et Materilia, Vol. 14, 1966, pp. 1349-1350.
31. N. Brown, "The Interaction between Dislocation and the Superlattice", Mechanical Properties of Intermetallic Compounds, Ed. J.H. Westbrook, John Wiley & Sons Inc., 1959, pp.177-191.
32. P. Veyssiere, J. Doudin and P. Beauchamp, "On the Presence of Superlattice Intrinsic Stacking Fault in Plastically Deformed Ni₃Al," Phil. Mag. A 51, 1985, pp. 469-483.

REFERENCES (cont.)

33. N.S. Stoloff, "Cyclic Deformation of Intermetallic Alloys," Ordered Intermetallic-Physical Metallurgy and Mechanical Behaviour, Eds. C.T. Liu et al, pp. 257-277.
34. A. Ball, "The Observations of a Martensitic Transformation in the Compound NiAl", Metal Science Journal, 1967, pp. 47-48.
35. R. W. Guard and A. M. Turkalo, "Fractographic Studies in NiAl and Ni₃Al", Mechanical Properties of Intermetallic Compounds", Ed. J.H. Westbrook, John Wiley & Sons Inc., 1959 pp. 141-160.
36. P. Nagpal et al, High Temperature Ordered Intermetallic Alloys IV, Eds. L. Johnson et al, MRS Proceedings, Vol. 213, 1991, pp. 533-534
37. Kaushik Bhattacharya, "The Microstructure of Martensite and its Implications on the Shape-Memory Effect", Micro-structure and Phase Transition", Eds. David Kinderlehrer et al, Springer-Verlag, 1992, 209-220.
38. Robert E. Reed-Hill, "Physical Metallurgy Principles", Ed. Reed-Hill, second edition, 1962.
39. C. Wayman, "The Geometry Observable in Martensitic Transformations", Introduction to the Crystallography of Martensitic transformation, Eds. Morris E. Fine et al, McMillian Co., 1964, pp . 76-83.
40. C. Wayman, "General Construction of Theory", Introduction to the Crystallography of Martensitic Transformation, Eds. Morris E. Fine et al, McMillian Co., 1964, pp.84-97.
41. D. Schryvers, "Multiply Twinned Phases and Microstructures in NiAl: A Transmission Electron Microscopy Study", Microstructure and Phase Transition, Springer-Verlay, Ed. David Kinderlehrer et al, 1984, pp. 143-152.
42. K. Enami, S. Nenno and K. Shimizu, "Crystal Structure and Internal Twins of the Ni-36.8 at. % Al Martensite", Transactions JIM, Vol. 14, 1973, pp. 161-165.

REFERENCES (cont.)

43. Y.D. Kim and C.M. Wayman, "Shape Recovery and Phase Transformation Behaviour in NiAl Alloys," Metallurgical Transactions - A, Vol. 23A, Nov. 1992, pp. 2981-2986.
44. C.M. Wayman and T.W. Duerig, "An Introduction to Martensite and Shape Memory", Eds. C.M. Wayman et al, Engineering Aspects of Shape Memory Alloys, Butterworth-Heinemann, 1990, pp.3-20.
45. D.Y. Li, "Wear Behaviour of Ti Ni Shape Memory Alloys", Scripta Materialia, Vol. 34, No. 2, 1996, pp. 195-200.
46. P. Lin et al, "Influence of Strain Rate on Deformation Properties of TiNi Shape Memory Alloys", ISME International Journal, Vol. 39, No. 1, Jan. 1996, pp. 117-123.
47. Y.K. Au and C.W. Wayman, "Thermoelastic Behaviour of the Martensitic Transformation in β NiAl Alloys", Scripta Metallurgica, Vol. 6, 1972, pp. 1209-1214.
48. T. E. Buchheit and J.W. Wert, "Predicting the Orientation-Dependent Stress-Induced Transformation and Detwinning response of Shape Memory Alloy Single Crystals," Metallurgical and Materials Transactions 'A', Vol. 27A, Feb. 1996, pp. 269-279.
49. S. Miyazaki, S. Kimura, K.Otsuka, Y. Suzuki, "The Habit Plane and Transformation Strains Associated with the Martensite Transformation in Ti-Ni Single Crystals", Scripta Metallurgica, Vol. 18, 1984, pp. 883-888.
50. C. M. Wayman and S. Chakravorty, "The Thermoelastic Martensitic Transformation in β NiAl Alloys: I Crystallography and Morphology," Metallurgical Transactions 'A', Vol. 7A, April 1976, pp. 555-568.
51. T. W. Duerig and R. Sadno, "An Engineers Perspective of Pseudoelasticity," Eds. T.W. Duerig et al, Engineering Aspects of Shape Memory Alloys; Butterworth-Heinemann Ltd., 1990, pp. 369-393.
52. Tomoyuki Kakeshita, Takashi Fukuda and Toshio Saburi, "Time Dependent Nature of the Athermal Martensite in Fe-Ni Alloys", Scripta Materialia, Vol. 34, No. 1, 1996, pp. 147-150.

REFERENCES (cont.)

53. S. Chakravorty and C.W. Wayman, "The Thermoelastic Martensitic Transformation in β NiAl Alloys: II Electron Microscopy", Metallurgical Transactions - A, Vol. 7A, April 1976, pp. 569-582.
54. S. Rosen and J. A. Goebel, "The Crystal Structure of Nickel-rich NiAl and Martensitic NiAl", Transactions of the Metallurgical Society of AIME, Vol. 242, April 1968, pp. 722-724.
55. S. Vaidya, S. Mahajan and C. M. Preece, "The Role of Twinning in the Cavitation Erosion of Cobalt Single Crystals", Metallurgical Transactions - A, Vol. 11A, July 1980, pp. 1139-1150.
56. Peter Filip and Karel Mazanec, "Influence of Work Hardening and Heat Treatment on the Substructure and Deformation Behaviour of TiNi Shape Memory Alloys," Scripta Metallurgica et Materialia, Vol. 32, No. 9, 1995, pp. 1375- 1380.
57. K. Enami, V. V. Martynov, T. Tomie, L. G. Khandros, S. Nenno, "Deformation Behaviour of Ni-Al L1₀ (3R) Martensite", Transactions of the Japan Institute of Metals, Vol. 22, No. 5, 1981, pp. 357-366.
58. Y. D. Kim and C. M. Wayman, Metallurgical Transactions - A, Vol. 23A, Nov. 1992, pp. 2981 - 2986.
59. A. Thiruvengadam, "Handbook of Cavitation Erosion", Prepared under Office of Naval Research, Department of the Navy (US), Contract No. N00014-73-C-0017 Nr, 1976, pp. 62-293.
60. D.A. Woodford, "Cavitation-Erosion-Induced Phase Transformations of Alloys", Metallurgical Transactions, Vol. 3, May 1972, pp. 1137-1145.
61. Patrick A. March, "Cavitation Erosion Resistance for Nickel and Iron Aluminides", Tennessee Valley Authority Engineering Laboratory, Report No. WR28-4-900-213, Sept. 1988.
62. "Standard Method of Vibratory Cavitation Erosion Test", Annual Book of ASTM Standards, ASTM G-32-92, Vol. 03.02, p. 187.
63. F. J. Heymann, "On the Time Dependence of the Rate of Erosion due to Impingement or Cavitation," Erosion by Cavitation or Impingement, ASTM STP No. 408, 1967, pp. 70-110.

REFERENCES (cont.)

64. Anthony W. Thompson, "Fracture of Intermetallics", Structural Intermetallics, Eds. R. Darolia, J.J. Leandowski, C.T. Liu, H.C. Martin, D.B. Miracle and M.V. Nathal, The Minerals, Metals and Materials Society, 1993, pp. 879-884.
65. R.H. Richman and W.P. McNaughton, "Correlation of Cavitation Erosion Behaviour with Mechanical Properties of Metals", Wear Vol. 140, 1990, pp. 68-82.
66. Y. Shao, P.C. Clapp and J.A. Rifkin, "Molecular Dynamics Simulation of Martensitic Transformations in NiAl", Metallurgical and Materials Transactions A, Vol. 27A, June 1996, pp. 1477-1489.
67. G.C. Gould, "Some Observations on Erosion by Cavitation and Impingement", Characterization and Determination of Erosion Resistance, ASTM STP 414, 1970, pp. 182-211.
68. J.M. Hobbs, "Experience with a 20 KHz Cavitation Test", Erosion by Cavitation or Impingement, ASTM STP 408, 1967, pp. 159-179.